arTs Università degli Studi di Trieste
Archivio della ricerca – postprint

Spectroscopic and photometric periods of six ultracompact accreting binaries

Matthew J. Green [1]★ Thomas R. Marsh,[1]★ Philip J. Carter [2] Danny Steeghs,[1] Elmé Breedt [3] V. S. Dhillon [4,5] S. P. Littlefair,[4] Steven G. Parsons [4] Paul Kerry,[4] Nicola P. Gentile Fusillo,[6] R. P. Ashley,[1] Madelon C. P. Bours,[1] Tim Cunningham,[1] Martin J. Dyer [4] Boris T. Gänsicke [1] Paula Izquierdo,[5,7] Anna F. Pala,[6] Chuangwit Pattama,[8] Sabrina Outmani,[1] David I. Sahman,[4] Boonchoo Sukaum[8] and James Wild [4]

[1]*Astronomy and Astrophysics Group, Department of Physics, University of Warwick, Coventry CV4 7AL, UK*
[2]*Department of Earth and Planetary Sciences, University of California Davis, One Shields Avenue, Davis, CA 95616, USA*
[3]*Institute of Astronomy, University of Cambridge, Madingley Road, Cambridge CB3 0HA, UK*
[4]*Department of Physics and Astronomy, University of Sheffield, Sheffield S3 7RH, UK*
[5]*Instituto de Astrofísica de Canarias, E-38205 La Laguna, Tenerife, Spain*
[6]*European Southern Observatory, Karl Schwarzschild Straße 2, Garching D-85748, Germany*
[7]*Departamento de Astrofísica, Universidad de La Laguna, E-38206 La Laguna, Tenerife, Spain*
[8]*National Astronomical Research Institute of Thailand (Public Organization), 260 Moo 4, Donkaew, Mae Rim, Chiang Mai 50180, Thailand*

ABSTRACT

Ultracompact accreting binary systems each consist of a stellar remnant accreting helium-enriched material from a compact donor star. Such binaries include two related sub-classes, AM CVn-type binaries and helium cataclysmic variables, in both of which the central star is a white dwarf. We present a spectroscopic and photometric study of six accreting binaries with orbital periods in the range of 40–70 min, including phase-resolved VLT spectroscopy and high-speed ULTRACAM photometry. Four of these are AM CVn systems and two are helium cataclysmic variables. For four of these binaries we are able to identify orbital periods (of which three are spectroscopic). SDSS J1505+0659 has an orbital period of 67.8 min, significantly longer than previously believed, and longer than any other known AM CVn binary. We identify a *Wide-field Infrared Survey Explorer (WISE)* infrared excess in SDSS J1505+0659 that we believe to be the first direct detection of an AM CVn donor star in a non-direct impacting binary. The mass ratio of SDSS J1505+0659 is consistent with a white dwarf donor. CRTS J1028–0819 has an orbital period of 52.1 min, the shortest period of any helium cataclysmic variable. MOA 2010-BLG-087 is co-aligned with a K-class star that dominates its spectrum. ASASSN-14ei and ASASSN-14mv both show a remarkable number of echo outbursts following superoutbursts (13 and 10 echo outbursts respectively). ASASSN-14ei shows an increased outburst rate over the years following its superoutburst, perhaps resulting from an increased accretion rate.

Key words: binaries: close – stars: dwarf novae – novae, cataclysmic variables – white dwarfs.

1 INTRODUCTION

Cataclysmic variables (CVs) are compact, interacting binaries. Each CV consists of a white dwarf accreting material from a donor star which fills its Roche lobe (Warner 1995). For non-magnetic systems, this accretion occurs via an accretion disc around the central white dwarf. In the vast majority of CVs, the donor closely resembles a main-sequence star at the point at which accretion starts. For such systems there exists a minimum orbital period, observed to be 79.6 ± 0.2 min (Knigge, Baraffe & Patterson 2011; McAllister et al. 2019). Accreting binaries that have orbital periods shorter than this limit must therefore have donors which were

★ E-mail: mjgreenastro@gmail.com (MJG); t.r.marsh@warwick.ac.uk (TRM)

not typical main-sequence stars at the point of first contact. The most common explanation is for the donor to be evolved, with a helium-rich nature and consequently greater density that allows the binary to exist at shorter orbital periods. CVs with evolved donors and periods shorter than the canonical period minimum can be divided into two sub-classes: helium-rich CVs (He CVs) that accrete helium-enriched material containing some amount of hydrogen, and AM Canum Venaticorum (AM CVn) type binaries, which accrete helium-dominated material with no detectable hydrogen. AM CVn binaries include the shortest period systems known (Motch et al. 1996; Israel et al. 1999; Steeghs et al. 2006; Roelofs et al. 2010), and are expected to be among the strongest Galactic sources of gravitational wave radiation in the LISA frequency range (Kremer et al. 2017; Breivik et al. 2018; Kupfer et al. 2018). Although He CVs and AM CVn binaries are similar in appearance, the extent to which they are evolutionarily related is not yet well understood.

The formation path of a He CV is as follows. In a volume-limited sample, 5 ± 3 per cent of CVs appear to have evolved donors (Pala et al. 2020). The majority of these donor stars still have hydrogen-dominated atmospheres and orbital periods longer than the canonical period minimum. Over time, mass transfer will strip away the atmosphere of the donor star, revealling the helium-enriched core. In this manner, the accreted material becomes helium-rich. At the same time, the increasing density of the donor star will require that the binary evolves to a shorter orbital period.

The evolution of AM CVn binaries is uncertain, with three proposed channels (see Solheim 2010 for an overview, and Green et al. 2018b and Ramsay et al. 2018 for recent results). In two of these channels, the binary goes through two phases of common envelope evolution (Ivanova et al. 2013), leaving either a double white dwarf binary (Paczyński 1967; Deloye et al. 2007), or a binary consisting of a white dwarf and a helium-burning star whose atmosphere has been stripped during the common envelope evolution (Savonije, de Kool & van den Heuvel 1986; Iben & Tutukov 1987; Yungelson 2008).

In the third suggested channel of AM CVn evolution, the AM CVn binary descends directly from a He CV in which the core of the donor star is sufficiently helium-enriched (Podsiadlowski, Han & Rappaport 2003; Goliasch & Nelson 2015). As a source of AM CVn binaries, this channel has several uncertainties. First, the region of initial parameter space for which a binary will be able to remove all detectable hydrogen from the accreted material is rather small, and many He CVs will never successfully remove enough hydrogen to become AM CVn binaries (Goliasch & Nelson 2015). As such we might expect the number of known, sub-period minimum He CVs to provide an approximate upper limit on the number of AM CVn binaries formed by this channel. Secondly, the majority of AM CVn binaries that do form by this channel are not expected to reach periods shorter than ≈45 min (Podsiadlowski et al. 2003; Goliasch & Nelson 2015). As a result, population synthesis models generally disfavour this model *for short period AM CVn binaries* compared to the two previously discussed, predicting a contribution of order a few per cent to the population of AM CVn binaries with periods $\lesssim$30 min (Nelemans, Yungelson & Portegies Zwart 2004; Goliasch & Nelson 2015). For AM CVn binaries with orbital periods $\gtrsim$45 min; however, this channel remains a viable option. Indeed, the most precise to date mass and radius measurements of an AM CVn donor star (from the first fully eclipsing AM CVn binary, Gaia14aae, which has an orbital period of 50 min) agree best with predictions based on the He CV channel (Green et al. 2018a, 2019).

Table 1. Properties of known CVs (not including AM CVn binaries) with orbital periods shorter than 79.6 min. The majority are He CVs, but note that the donor of SDSS J1507+5230 does not appear to be evolved; instead, its orbital period can be explained by the low metallicity (and hence increased density) of its halo-population donor star. CRTS J0808+3550 and CRTS J1647+4338 do not have measured orbital periods, but are believed to be below the orbital period minimum due to the low hydrogen content of their accreted material. In the case of V485 Cen, q is derived from spectroscopic studies of dynamics; for all other systems q is derived from the superhump relationship. In these cases, we have recalculated q from the Stage B superhump excess using equation (2). *References:* [1] Kato et al. (2009); [2] Woudt et al. (2012); [3] Carter et al. (2013); [4] Littlefield et al. (2013); [5] Ramsay et al. (2014); [6] Augusteijn, van Kerkwijk & van Paradijs (1993); [7] Augusteijn et al. (1996); [8] Woudt & Warner (2011); [9] Thorstensen et al. (2002); [10] Chochol et al. (2015); [11] Imada et al. (2018); [12] Breedt et al. (2012); [13] Kato et al. (2015b); [14] Szkody et al. (2005); [15] Uthas et al. (2011); [16] VSNET alert 19922; [17] VSNET alert 21021; [18] VSNET alert 21588; [19] Breedt et al. (2014). Note that a number of these measurements have not been confirmed by any peer-reviewed source.

Name	Period (min)	q	Ref
CRTS J1028−0819	52.1	0.25 ± 0.06	1,2
SBSS 1108+574	55.3	0.085 ± 0.015	3,4
BOKS45906	56.4	–	5
V485 Cen	59.0	0.38 ± 0.13	6,7
CRTS J2333−1557	62.0	–	8
EI Psc	64.2	0.185 ± 0.007	9
CRTS J1740+4147	64.8	0.055 ± 0.006	10,11
CRTS J1122−1110	65.2	0.020 ± 0.007	12
V418 Ser	65.9	–	13
SDSS J1507+5230	67	–	14,15
ASASSN-16fy	70.9	–	16
ASASSN-17gf	76.6	–	17
ASASSN-17ou	79.5	–	18
CRTS J0808+3550	–	–	19
CRTS J1647+4338	–	–	19

Further attempts to study the prior evolution of these binaries are limited by the small numbers of such systems which are amenable to characterization. Key properties to constrain the prior evolution of a binary are its orbital period ($P_{\rm orb}$) and the ratio of masses of its two stars ($q = M_2/M_1$, where M_1 is the mass of the accretor and M_2 is the mass of the donor). At present, 56 AM CVn binaries (Ramsay et al. 2018) and 13 sub-period minimum He CVs (see Table 1) are known. Another two He CVs are believed to be below the period minimum due to the low hydrogen content of their accreted material. However, many systems of both classes are too faint for detailed follow-up. Only 33 AM CVn binaries have published, directly measured orbital periods (and references therein Green et al. 2018b). Note that this number does not include those systems for which an indirect estimate of the orbital period has been made, based either on its superhump period (see the discussion in the following section) or on its outburst properties (Levitan et al. 2015). Only 17 AM CVn binaries (Green et al. 2018b) and six sub-period minimum He CVs (Table 1) have published mass ratio measurements.

In this paper, we present a spectroscopic and photometric study of six short-period accreting binaries, including four AM CVn binaries and two sub-period minimum He CVs (Table 2). Our goal is to use these data to measure the orbital periods and, where possible, mass ratios of these systems, in the hope of exploring their prior evolution.

Table 2. Targets observed for this work. Magnitudes are taken from *Gaia* DR2 (Gaia Collaboration 2018) and are given in the *G* band, except where otherwise stated. Parallaxes are from *Gaia* DR2, and distances are calculated using the method described by Kupfer et al. (2018). We have avoided the *Gaia* magnitude of ASASSN-14ei as it is significantly discrepent from the CRTS *V* magnitude (at $G = 16.4$). See Section 3.3.1 for a discussion of this discrepancy.

Target	Coordinates (J2000)	Class	Quiescent mag.	Outburst	Parallax (mas)	Distance (pc)
SDSS J1505+0659	15:05:51.58 + 06:59:48.7	AM CVn	19.1	–	6.3(5)	160 ± 12
ASASSN-14ei = OX Eri	02:55:33.39 – 47:50:42.0	AM CVn	$V = 18.0$	$V = 11.9$	3.92(5)	255 ± 4
ASASSN-14mv = V493 Gem	07:13:27.28 + 20:55:53.4	AM CVn	18.0	$V = 12.8$	4.07(12)	247 ± 7
MOA 2010-BLG-087	18:08:34.85 – 26:29:22.8	AM CVn	19.4	$V \approx 14.7$	–	–
CRTS J1028–0819	10:28:42.89 – 08:19:26.6	He CV	19.4	$V = 14.8$	1.4(3)	720 ± 200
V418 Ser	15:14:53.64 + 02:09:34.5	He CV	20.2	$V = 15.8$	0.5(6)	1200 ± 300

1.1 Photometric behaviour

We start with a brief overview of the photometric behaviour of CVs and AM CVn binaries, as these binaries exhibit a range of phenomena on various time-scales.

Both CVs and AM CVn binaries undergo brightening events known as dwarf nova outbursts. These outbursts are caused by an instability in the temperature and density of the accretion disc, causing the material to temporarily ionize, which in turn causes the system to brighten by ∼2–9 mag. This brightening can last of order days to weeks. The outbursts of hydrogen- and helium-dominated discs are broadly similar, though different in some specifics (Lasota 2001; Kotko et al. 2012; Cannizzo & Nelemans 2015). In short-period CVs and AM CVn binaries, the outbursts that are seen generally belong to the subtype of dwarf nova outbursts known as 'superoutbursts' (Kotko et al. 2012). Superoutbursts generally last for weeks, and are brighter on average than a typical outburst. Following a superoutburst, some CVs and AM CVn binaries show a series of 'echo outbursts', which resemble ordinary dwarf nova outbursts. These are thought to be the result of reflections within the disc of the transition waves that mediate the change from ionized to neutral disc states (Patterson et al. 1998; Meyer & Meyer-Hofmeister 2015).

Among AM CVn binaries, there is a steep dependence between the orbital period of the binary and the mass transfer rate, which in turn drives the behaviour of the accretion disc. Empirical relations exist between the outburst properties and the orbital period of the binary (Cannizzo & Nelemans 2015; Levitan et al. 2015; Cannizzo & Ramsay 2019). The tightest of these correlations, relating the recurrence time between outbursts to the orbital period, is given by

$$\tau_{\rm recur} = (1.53 \times 10^{-9}) P_{\rm orb}^{7.35} + 24.7\,{\rm d}, \quad (1)$$

based on a sample of 11 outbursting AM CVn binaries with orbital periods between 22 and 37 min (Levitan et al. 2015). Outbursts are rarely seen for systems with periods longer than 50 min.

On time-scales of minutes to hours, CVs and AM CVn binaries show a variety of photometric signals. Some of these may be quasi-periodic variability originating in the disc (Fontaine et al. 2011; Kupfer et al. 2015). However, many CVs and some AM CVn binaries show a photometric signature coincident with the orbital period of the binary (Armstrong, Patterson & Kemp 2012; Green et al. 2018b). Alongside this, many AM CVn binaries and short-period CVs show a photometric signature known as the 'superhump' period. The signal is most often visible during superoutburst, and is coincident with a beat frequency between the orbital period and the precession period of an eccentric disc (Patterson et al. 2005). This superhump period is generally a few per cent longer than the orbital period. The disc precession itself is sometimes seen photometrically (Green et al. 2018b), but as the time-scale is of order 12 h such detections are often not possible from single-site, ground-based photometry.

The precession of the disc is driven by the tidal pull of the donor star. An empirical relationship exists between the superhump period, the orbital period, and the mass ratio of the two stars (Patterson et al. 2005; Knigge 2006; Kato & Osaki 2013). Various forms of the relationship are given in the literature. For this work, we will use the expression given by McAllister et al. (2019). This expression includes uncertainties on the relationship itself, following the form of Knigge (2006) but using a larger sample of systems. For stage B superhumps and a sample of 24 systems, McAllister et al. (2019) gives

$$q(\epsilon) = (0.118 \pm 0.003) + (4.45 \pm 0.28) \times (\epsilon - 0.025), \quad (2)$$

where $\epsilon = (P_{\rm sh} - P_{\rm orb})/P_{\rm orb}$, and $P_{\rm sh}$ and $P_{\rm orb}$ are the superhump and orbital periods, respectively. For stage C superhumps and a sample of 15 systems, they give a different relationship of

$$q(\epsilon) = (0.135 \pm 0.004) + (5.0 \pm 0.7) \times (\epsilon - 0.025). \quad (3)$$

See Kato et al. (2009) for a discussion of the differences between superhump stages. It should be noted that these relationships were calibrated based on hydrogen-accreting CVs, and doubts have been raised as to whether such a relationship can be extended to the helium-dominated discs of He CVs or AM CVn binaries (Pearson 2007). For the two AM CVn systems where q has been measured by both superhump and alternate methods, one is in agreement and the other is not (Roelofs et al. 2006; Copperwheat et al. 2011). Regardless, these relationships are widely used to characterize AM CVn binaries where other methods of measuring q are not possible (Roelofs et al. 2006; Armstrong et al. 2012; Isogai et al. 2019).

2 OBSERVATIONS

The targets for these observations were selected from known but poorly characterized accreting binaries believed to have orbital periods shorter than the period minimum. While all have been included in previously published lists of short-period binaries (e.g. Breedt 2015; Ramsay et al. 2018), several have no peer-reviewed data available and none have been the subject of detailed follow-up before now. A summary of all observations presented in this work is presented in Table 3.

2.1 VLT spectroscopy

Five targets were observed using the 8.2 m Very Large Telescope (VLT) at Paranal Observatory, Chile, under observing proposal 095.D-0888. Fainter targets ($G > 19.5$) were observed by FORS2 (the FOcal Reducer and low dispersion Spectrograph), a spectrograph with lower dispersion (Appenzeller et al. 1998). Brighter

Table 3. Observations presented in this paper. For spectroscopic observations we give the wavelength range, while we give the filter for photometric observations.

Target	Instrument	Date	Wavelength range or filter	Exposure (s)
Spectroscopy				
SDSS J1505+0659	VLT + X-shooter	2015 Apr 9	3200–10 100 Å	16 × 300
ASASSN-14ei	VLT + X-shooter	2015 Aug 11	3200–10100 Å	22 × 240
ASASSN-14mv	WHT + ISIS	2019 Feb 23	3850–4600, 5750–9000 Å	2 × 800 + 5 × 600
MOA 2010-BLG-087	VLT + FORS2	2015 May 14	3850–6300 Å	10 × 240
CRTS J1028–0819	VLT + X-shooter	2015 Apr 9	3200–10 100 Å	18 × 300
V418 Ser	VLT + FORS2	2015 Apr 9	3850–6300 Å	21 × 240
Photometry				
SDSS J1505+0659	TNT + ULTRASPEC	2014 Jan 27	*KG5*	207 × 10
	NTT + ULTRACAM	2019 Mar 28	$u_s g_s r_s$	616 × 10
ASASSN-14ei	NTT + ULTRACAM	2018 Jan 18	$u_s g_s r_s$	785 × 10
		2018 Nov 09	$u_s g_s r_s$	2782 × 5
		2018 Nov 10	$u_s g_s r_s$	3030 × 5
		2018 Nov 12	$u_s g_s r_s$	2952 × 5
ASASSN-14mv	TNT + ULTRASPEC	2015 Jan 04	*g'*	6910 × 1
		2015 Jan 05	*g'*	1923 × 1 + 5047 × 0.5
		2017 Dec 14	*KG5*	754 × 10
		2018 Feb 08	*KG5*	1346 × 10
		2018 Feb 09	*KG5*	1278 × 10
MOA 2010-BLG-087	NTT + ULTRACAM	2010 Apr 21	*u'g'r'*	502 × 5.6
		2010 Apr 22	*u'g'r'*	1866 × 5.6
		2010 Apr 24	*u'g'r'*	1932 × 5.6
V418 Ser	NTT + ULTRACAM	2018 Apr 15	$u_s g_s r_s$	597 × 15

targets were observed by X-shooter and an Echelle spectrograph (Vernet et al. 2011). Each target was observed continuously for 2 h.

Observations with FORS2 were carried out using the 600B grism and a slit width of 1 arcsec, giving a resolution ($\lambda/\Delta\lambda$) of 780. Spectra were reduced using PAMELA and MOLLY (Marsh 2019).[1] Each frame was bias-subtracted and flat-corrected using tungsten lamp flats. Sky lines were subtracted, and fluxes were extracted using optimal weights (Marsh & Horne 1988). Wavelength calibrations were performed using a HgCd arc lamp observed the preceding day. Data were flux calibrated against spectrophotometric standard stars observed the same night: LTT 7379 in both cases.

X-shooter observations were carried out using a slit width of 1.2 arcsec in the VIS arm (5500–10 200 Å) and 1 arcsec in the UVB arm (3200–5500 Å), producing resolutions ($\lambda/\Delta\lambda$) of 6500 and 5400, respectively. Data from the near-infrared arm of X-shooter were not used due to the blue nature of these objects. X-shooter data were reduced using the standard X-shooter pipeline produced by ESO (REFLEX).

2.2 William Herschel Telescope (WHT) spectroscopy

A further target, ASASSN-14mv, was observed using the Intermediate-dispersion Spectrograph and Imaging System (ISIS) instrument on the 4.2 m WHT. This target was observed for approximately 75 min. ISIS has two optical arms with adjustable central wavelengths. One spectrum was taken with the arms centred on 3900 and 8200 Å, to search for calcium and nitrogen, and a further six with the arms centred on 4500 and 6600 Å. The R600B and R600R gratings were used, with a GG495 order-sorting filter in the red arm. The slit width was 1.2 arcsec, giving a resolution of 9200. These spectra were also reduced using PAMELA and MOLLY, using the same procedure as described above for FORS2. Wavelength calibrations were carried out using a CuNe + CuAr arc lamp observed before and after the target, and the flux was calibrated using the standard star LTT 7379.

2.3 Survey photometry

To characterize the outburst behaviour of these systems, we retrieved data from public-access photometric surveys, including the American Association of Variable Star Observers (AAVSO), the Catalina Real-time Transient Survey (CRTS; Drake et al. 2009), the Palomar Transient Factory (PTF; Rau et al. 2009), the Zwicky Transient Facility (ZTF, Masci et al. 2019), the Panoramic Survey Telescope and Rapid Response System (Pan-STARRS; Chambers et al. 2016), and the All-Sky Automated Search for SuperNovae (ASAS-SN; Shappee et al. 2014; Kochanek et al. 2017).

Observations of several of our targets have previously been reported through the Variable Star Network (VSNET; Kato et al. 2004). We reference the appropriate VSNET alerts where relevant.

2.4 High-speed photometry

Where possible, we collected high-speed photometry of these targets using the cameras ULTRACAM and ULTRASPEC (Dhillon et al. 2007, 2014). ULTRACAM is a triple-beam imaging photometer which uses frame-transfer CCDs to reduce dead time between exposures to negligible amounts (≈25 ms). For these observations, it was mounted on the 3.5 m New Technology Telescope (NTT) at La Silla Observatory, Chile. For earlier observations the standard Sloan *u'g'r'* filters were used in the three beams. For more recent observations, custom $u_s g_s r_s$ filters were used (Dhillon et al. 2018), designed to replicate the wavelength ranges of the standard filters but with a higher throughput (especially in the u_s band). ULTRASPEC is a single-band imaging photometer which also uses frame-transfer

[1] http://deneb.astro.warwick.ac.uk/phsaap/software/

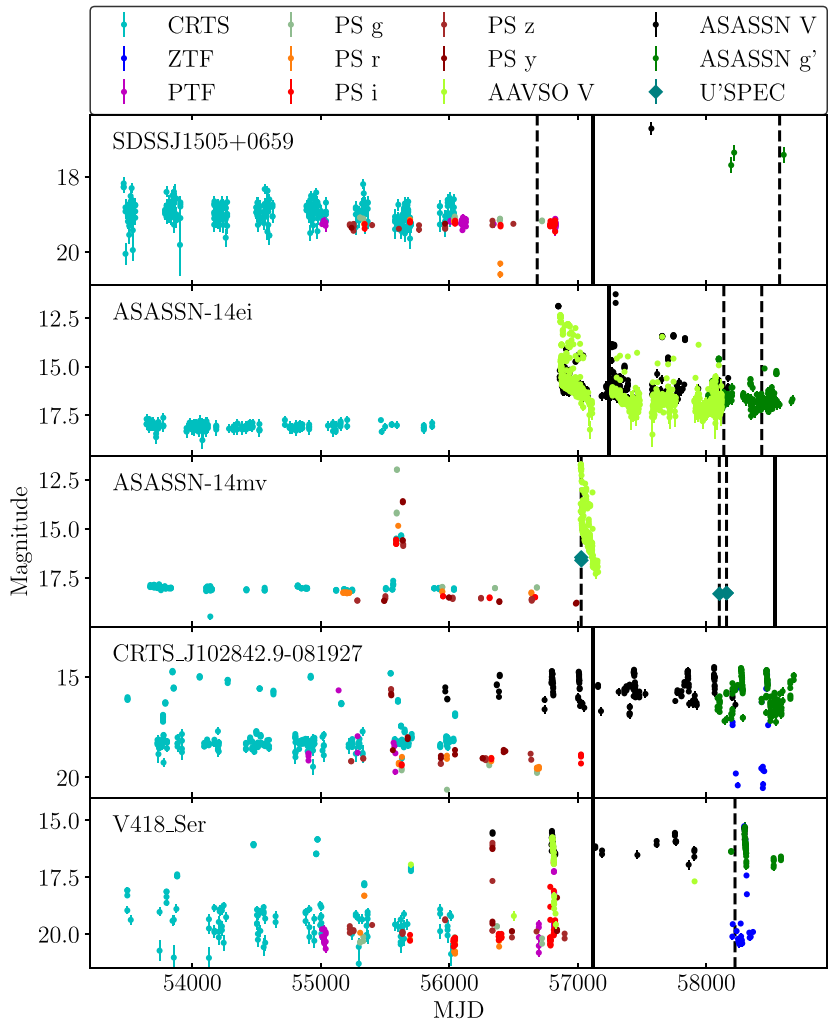

Figure 1. Long-term light curves of the systems presented in this paper, except for MOA 2010-BLG-087. Vertical lines represent the times of our observations, either spectroscopy (solid) or high-speed photometry (dashed). Note that we have not shown the ASAS-SN detections of ASASSN-14 mv, due to the spurious 1.5 mag offset discussed in Section 3.3.1. Several targets have spurious ASAS-SN detections that coincide with the limiting magnitude of ∼17; most notably this includes the bright points of SDSS J1505+0659.

CCDs. It is mounted on the 2.5 m Thai National Telescope (TNT) on Doi Inthanon, Thailand. For some observations the *g'* band was used, while for other observations we used the custom *KG5* filter, a broad filter approximately equal to $u' + g' + r'$, chosen for its greater throughput (see Hardy et al. 2017, Appendix A).

Data were reduced using the standard ULTRACAM pipeline. Each frame was bias- and dark-subtracted. Pixel sensitivity was corrected for using sky flats observed on the same night where available, otherwise using sky flats observed at another time during the observing run. Fluxes were extracted using a variable-width aperture of radius 1.7 × the full-width half-maximum of the point spread function of stars in that frame, with pixel fluxes weighted optimally (Naylor 1998). Each flux was divided by that of a nearby, non-variable comparison star to correct for atmospheric transparency variations. Solar system barycentric time corrections were applied to account for light traveltime and time dilation.

The fluxes of the comparison stars were taken from the Sloan Digital Sky Survey (SDSS) or from the AAVSO Photometric All-Sky Survey (APASS). Comparison stars used were at 15:05:49.3 + 06:57:02.7 ($g' = 15.90$ mag from SDSS) for SDSS J1505+0659; 02:55:33.1–47:53:10.9 ($g' = 15.94$ mag from APASS) for ASASSN-14ei; 07:13:22.8 + 20:55:17.5 ($g' = 16.22$ mag from APASS) for ASASSN-14mv; and 15:15:00.6 + 02:09:05.6 ($g' = 16.35$ mag from SDSS) for V418 Ser. For MOA 2010-BLG-087, we used a comparison star at 18:08:35.3–26:29:14.7 for atmospheric corrections. As no SDSS or APASS magnitude is available due to the crowded nature of the field, we flux-calibrated these data using a standard star (Ru 152) observed on the same night. Note that for the $u_s g_s r_s$ filters used for much of the data, flux calibration is only approximate: this is especially true for the u_s band, where magnitudes can differ by ∼0.1 mag from the corresponding *u'* magnitude. As our photometric data are used only for timing purposes, such approximate calibrations are sufficient.

3 RESULTS

Long-term light curves of each system are shown in Fig. 1. Average spectra of each object are shown in Figs 2 (objects observed with X-shooter), 3 (objects observed with FORS2), and 4 (the object observed with ISIS). In Fig. 5, we show line profiles for the 5876 Å He I line in each system, along with other lines of interest.

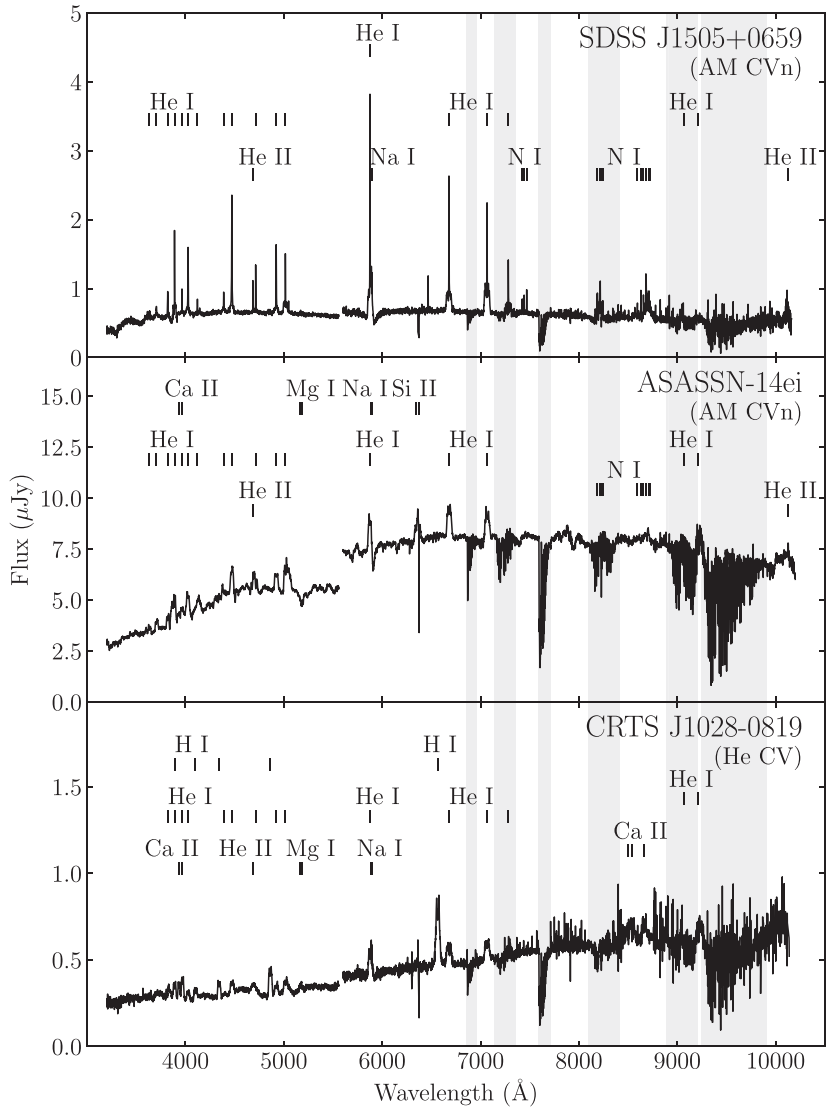

Figure 2. Average spectra of systems observed with X-Shooter on the 8.2 m VLT. Identified spectral features have been labelled. Grey shaded regions are dominated by telluric absorption, which has not been corrected for. Data have been rebinned by a factor of 5.

3.1 SDSS J1505+0659

SDSS J1505+0659 is a known AM CVn binary discovered by Carter et al. (2014). The system was discovered as part of a spectroscopic survey for AM CVn systems, selecting targets according to their SDSS colours (Carter et al. 2013). The discovery paper included four spectra of the system retrieved from the SDSS data base, from which they suggested an orbital period of 50.6 min. The uncertainties on their measured radial velocities (RVs) were large compared to the amplitude of the variation, due to the low resolution of SDSS spectra. Given this and the small number of data points available at the time, the orbital period was considered preliminary and subject to significant uncertainty.

3.1.1 Spectroscopy

Our combined VLT spectrum of SDSS J1505+0659 is shown in Fig. 2. The spectrum consists of a series of narrow helium emission lines imposed on a blue continuum. The profile of these helium emission lines is dominated by a strong central spike emission feature with relatively weak emission wings (Fig. 5). Central spike features are seen in many AM CVn binaries, and are emitted from on or near the surface of the accreting white dwarf (Green et al. 2019), though the emission mechanism is uncertain. As was noted by Carter et al. (2014), the strength of the central spike emission seen here is similar to a number of other long-period AM CVn binaries, including SDSS J1208+3550 (orbital period 53.0 min; Kupfer et al. 2013), SDSS J1137+4054 (59.6 min; Carter et al. 2014), and V396 Hya (65.1 min; Ruiz et al. 2001; Kupfer et al. 2016).

Emission features are seen from nitrogen and sodium (we show the latter in Fig. 5). The presence of nitrogen emission is reminiscent of GP Com (46.5 min; Nather, Robinson & Stover 1981; Marsh et al. 1990; Kupfer et al. 2016) and V396 Hya (Kupfer et al. 2016). The Na I emission is single-peaked and does not undergo any measurable velocity excursions. As such, we suggest it may share an origin with the He I and He II central spikes. (Given the weaker strength of the Na I lines, it is unlikely that the small velocity excursions

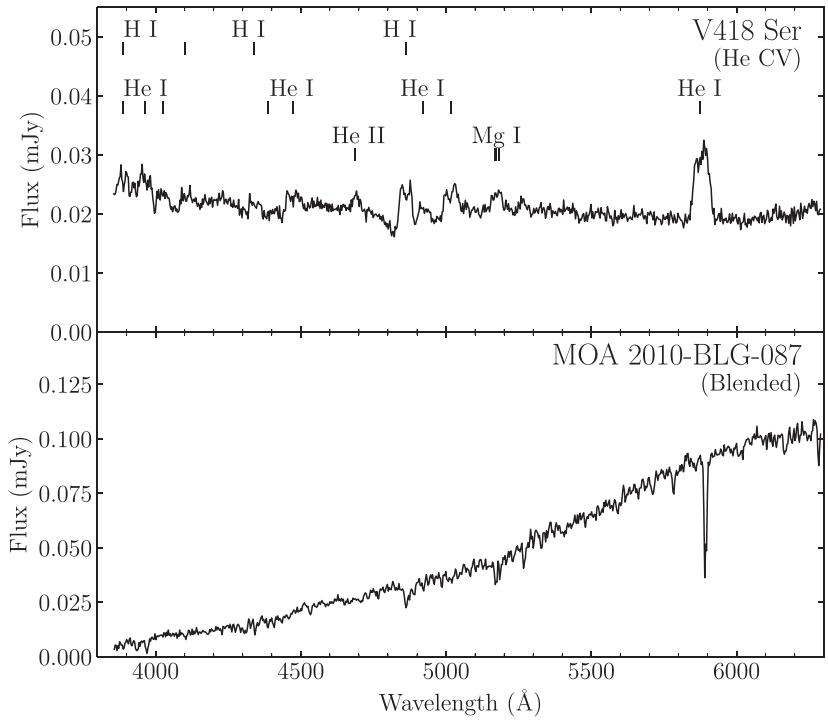

Figure 3. Average spectra of systems observed with FORS2 on the 8.2 m VLT. Identified spectral features have been labelled. As discussed in the text, MOA 2010-BLG-087 is blended with a nearby G- or K-star that dominates the spectrum. Data have been rebinned by a factor of 2.

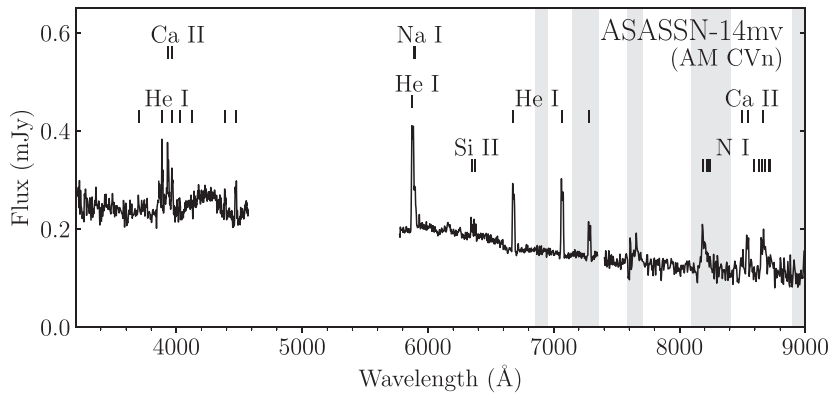

Figure 4. Average spectrum of ASASSN-14 mv, observed with ISIS on the 4.5 m WHT. Identified spectral features have been labelled. Grey shaded regions are dominated by telluric absorption, which has been corrected for. Data have been rebinned by a factor of 5.

of the central spike, discussed below, would be detected for Na I.) It is difficult for neutral sodium and ionized helium to exist at the same temperature range, suggesting that the origin of the central spike emission must be sufficiently extended to include a range of temperatures. In addition, we find a broad absorption feature centred on the Na I 5890–5895 Å doublet. Absorption of this breadth is likely to be photospheric in origin. This suggests a cool accreting white dwarf, as it is difficult to reconcile Na I absorption with an atmosphere hotter than $\sim$ 10 000 K.

The detection of sodium combined with a non-detection of calcium is unusual, and is worthy of note as it suggests that atmospheric sodium has been enhanced to levels higher than solar. This may provide insight into the prior nature of the donor star. Sodium can be produced via the Ne–Na cycle in the cores of high-mass main-sequence stars (Denisenkov & Ivanov 1987) or in the helium-burning shells of asymptotic giant branch stars (Mowlavi 1999). On the other hand, it should be noted that isolated sodium has been seen in at least one accreting binary with an unevolved, brown dwarf donor (Longstaff et al. 2019).

The central spike feature undergoes periodic, low-amplitude velocity excursions, as shown in the trailed spectrum (Fig. 6). These excursions were measured by cross-correlating each of the eight strongest emission lines in each spectrum with a Gaussian function. The RVs measured in this way follow a sinusoidal modulation with a semi-amplitude of $5.0 \pm 0.2\,\mathrm{km\,s^{-1}}$, around a systemic velocity (γ) that varies between different emission lines. In other AM CVn binaries, central spike γ values have been explained as a combination of an overall gravitational redshift and

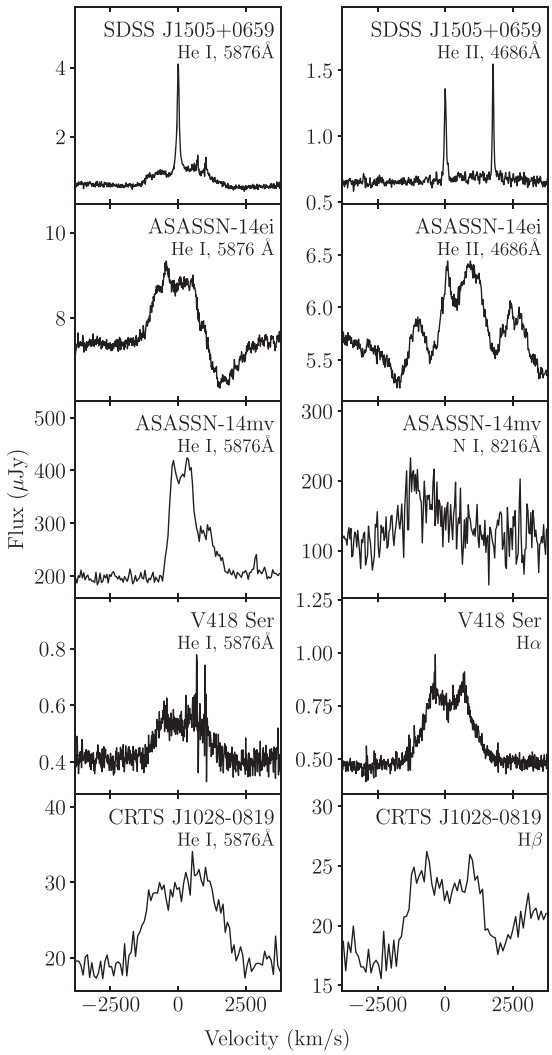

Figure 5. Profiles of He I 5876 Å lines for all five systems (left column), and of other spectral features of interest (right column). In windows centred on the He II 4686 Å line and the He I 4713 Å line can also be seen.

wavelength-dependent blueshifts arising from the Stark effect (Morales-Rueda et al. 2003; Kupfer et al. 2016; Green et al. 2019). We performed an initial sinusoidal fit to the measured RVs for each line individually, in order to measure γ for each line. The values of γ measured in this way are shown in Table 4. These γ values were then subtracted from the RVs in order to perform a combined sinusoidal fit to all emission lines.

The γ-subtracted data and their best-fitting sinusoid are shown in Fig. 7, along with a Lomb–Scargle periodogram (Lomb 1976; Scargle 1982; VanderPlas 2018). The sinusoidal fit was produced using a Markov Chain Monte Carlo method (MCMC; Goodman & Weare 2010; Foreman-Mackey et al. 2013). The nominal uncertainties on individual RV measurements were underestimated, as evidenced by a reduced χ^2 value of significantly more than one. We compensated for this by combining the individual uncertainties in quadrature with an additional uncertainty term. This term was included as a parameter in the MCMC, with a log-uniform prior. In Fig. 7, the uncertainties on the RV measurements have been scaled to include this additional uncertainty. The orbital period produced by this process is 67.8 ± 2.2 min.

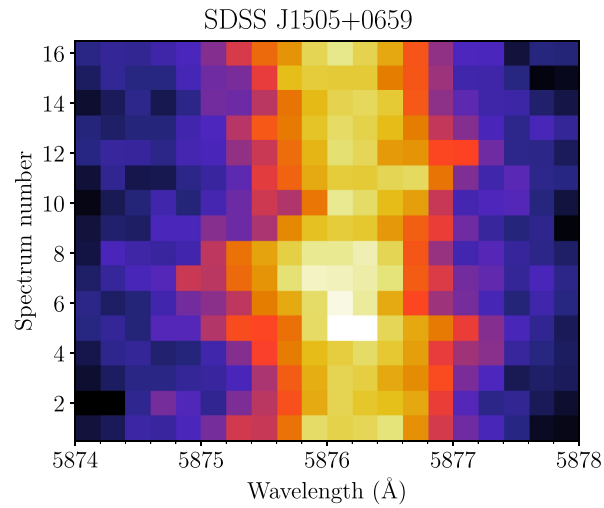

Figure 6. Trailed spectra of the He I 5875.6 Å line in SDSS J1505+0659, spanning a time period of 120 min, and showing the velocity excursions of the central spike. Note that the spike is slightly redshifted from its rest wavelength, as is commonly seen.

Table 4. Measured systemic radial velocities for the He I and He II lines of SDSS J1505+0659. These systematic velocity shifts were measured using a sinusoidal fit to the measured radial velocities.

Wavelength (Å)	γ (km s^{-1})
He I 4471	39.5 ± 1.0
He II 4686	25.1 ± 1.1
He I 4713	37.8 ± 2.0
He I 5015	21.3 ± 1.6
He I 5876	23.8 ± 0.7
He I 6678	27.5 ± 1.3
He I 7065	30.2 ± 1.5
He I 7281	28.9 ± 2.0

This newly measured period is significantly different from the 50.6 min period suggested by Carter et al. (2014). Given the uncertainties on their individual RV measurements, this discrepancy is not surprising. This is the longest orbital period of any known AM CVn binary – the longest previously published orbital period is that of V396 Hya at 65.1 ± 0.7 min (Ruiz et al. 2001).

When compared to the empirical correlation between orbital period and emission line strength noted by Carter et al. (2013), SDSS J1505+0659 is a clear outlier. For the He I 5876 Å line, we measure an equivalent width (EW) of −37.9 ± 3.2 Å. For a system with an orbital period of 68 min, Carter's relation would predict an EW of approximately −90 Å. However, there are several other systems with smaller EWs than would be predicted by the correlation, including SDSS J1208+3550 and SDSS J1137+4054. The unexpectedly weak EW of SDSS J1505+0659 may suggest that the disc is unusually weak. There is also likely to be an inclination dependence in the EW which may cause systems to be outliers.

3.1.2 Mass ratio

The mass ratio can be calculated from a combination of other binary properties: the orbital period ($P_{\rm orb}$), the velocity amplitude (K_1), the orbital inclination (i), and the mass of the accretor (M_1). The

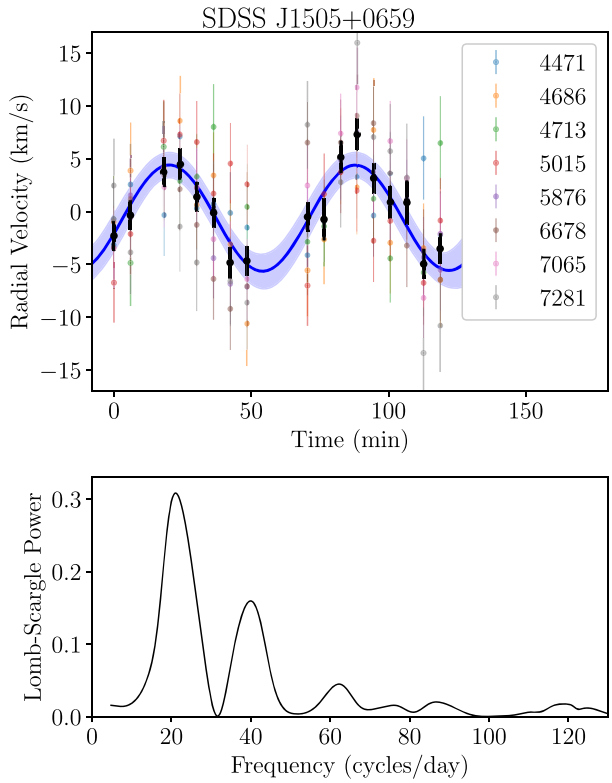

Figure 7. *Above:* Weighted mean RV measurements of SDSS J1505+0659 are shown as black points, while measurements from individual lines are shown as faded, coloured points. The median sinusoidal fit and 2σ range from a Markov chain Monte Carlo sampler is shown in blue, with a best-fitting period of 67.8 min. Uncertainties on RV measurements have been increased, as discussed in the text. *Below:* Lomb–Scargle plot produced from the measured RVs.

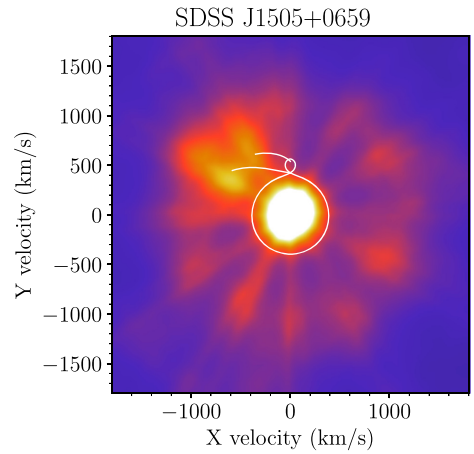

Figure 8. Doppler map of SDSS J1505+0659 produced from the 5015 Å He I line, and rotated to the standard orientation based on the RV fit in Fig. 7. Emission is dominated by the bright central spike, but an accretion disc and a bright-spot can also be seen. Radial spokes are an artefact of poor phase coverage. The superimposed white lines show predicted positions of various components, including: the Roche lobes of the two stars (the lobe of the accretor centred approximately on zero, and the donor star above this, centred on approximately $V_y = 450\,\mathrm{km\,s^{-1}}$); the velocities of a ballistic stream of infalling matter; and the Keplerian velocities at each point along the stream. The latter two are shown at positions beginning from the inner Lagrange point and ending at a radius of 0.7 times the Roche lobe radius.

calculation uses Kepler's law and the necessity that orbital velocity $v_1 = K_1/\sin i = 2\pi r/P_{\rm orb}$, where r is the separation of the accreting star from the centre of mass of the system. We have measurements of $P_{\rm orb} = 67.8 \pm 2.2$ min and $K_1 = 5.0 \pm 0.2\,\mathrm{km\,s^{-1}}$ from the sinusoidal fit shown in Fig. 7. For M_1, we assumed $0.8 \pm 0.1 M_\odot$. This value is typical of CV accretors (Pala et al. 2020) and consistent with the two AM CVn accretors that have measured masses (Copperwheat et al. 2011; Green et al. 2018a).

In order to constrain the orbital inclination, we measured the velocity of the peak intensity of the disc-originating emission line wings (i.e. the outer two peaks of the triple-peaked line profile). The peak intensity occurred at $v_D = 750 \pm 250\,\mathrm{km\,s^{-1}}$. This peak emission originates from close to the edge of the accretion disc, at a radius described by (Smak 1981; Warner 1995)

$$v_D^2 = \frac{M_1 G \sin^2(i)}{r_{\rm d}(0.95 \pm 0.05)^2}. \quad (4)$$

In this equation $r_{\rm d}$ is the disc radius and G is the gravitational constant. We assume that the disc radius is equal to 0.7 times the radius of the Roche lobe of the accretor, as is often seen in CVs (Warner 1995) and in the eclipsing AM CVn, Gaia14aae (Green et al. 2018a). The Roche lobe radius as a fraction of the orbital separation of the two stars (a) can be calculated as (Eggleton 1983)

$$\frac{R_L}{a} = \frac{0.49 q^{-2/3}}{0.6 q^{-2/3} + \ln(1 + q^{-1/3})}. \quad (5)$$

We combined these constraints using a MCMC routine. The median result was $q = 0.011^{+0.003}_{-0.001}$, where the uncertainties refer to the 16th and 84th percentiles of the distribution. The corresponding inclination was $i = 60 \pm 20^\circ$. This mass ratio is similar to that of V396 Hya, the previously longest-period AM CVn binary, which has $q = 0.014 \pm 0.004$ (Kupfer et al. 2016).

A Doppler map of the system was produced using the 67.8 min orbital period. The He I 5015 Å line was chosen because it has prominent disc emission. The Doppler map is shown in Fig. 8. The quality of this map is limited by the small number of spectra, giving the map spoke-like artefacts. Despite this, several features can be distinguished. In addition to the central spike and disc emission, a bright-spot can be seen in the top left quadrant. As this is the standard location for the bright-spot in Doppler maps, it provides further support to the RV measurements of the central spike that define the orbital phase. Fig. 8 also shows predicted velocity tracks for the infalling matter stream, based on the values from our MCMC fit, which approximately coincide with the bright-spot.

3.1.3 *Photometry*

The long-term light curve of SDSS J1505+0659 (Fig. 1) shows no activity over the period monitored. There are several ASAS-SN detections that are brighter than the baseline. However, as each is an isolated detection preceded and followed by non-detections, and consistent with the magnitude limit of ASAS-SN, we believe these to be false detections. For an AM CVn of this orbital period, outbursts are not expected due to the low-accretion rate.

In high-speed photometry of the system we detect no significant variability. By injecting a sinusoidal signal at the orbital period, and assuming that we would detect any signal that had a Lomb–Scargle peak at four times the mean Lomb–Scargle power, we estimate an

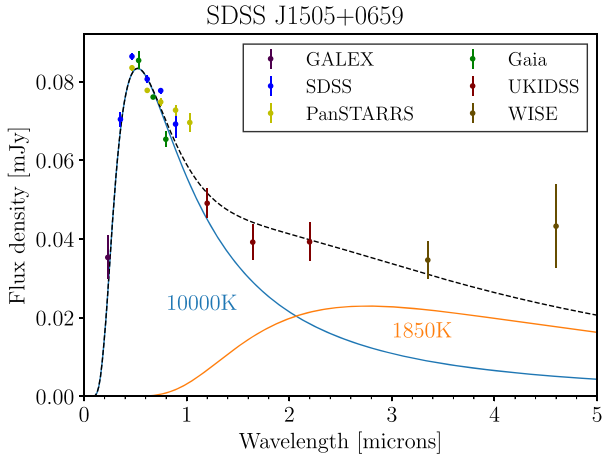

Figure 9. Spectral energy distribution of SDSS J1505+0659. The blue curve shows a blackbody spectrum at a temperature estimated from the optical fluxes, corrected for the predicted amount of reddening. The orange curve shows a second blackbody spectrum with radius fixed to the Roche lobe radius of the donor star, and the black dashed curve shows the sum of the two blackbody spectra. The addition of the second blackbody explains the infrared excess seen in the UKIDSS and *WISE* data.

upper limit on any orbital signal amplitude at 0.5 per cent of the system brightness.

The spectral energy distribution (SED) of SDSS J1505+0659 is noteworthy. In Fig. 9, we show flux densities measured by SDSS (Abazajian et al. 2009), *Gaia* (Gaia Collaboration 2018), Pan-STARRS (Chambers et al. 2016), the Galaxy Evolution Explorer (*GALEX*; Morrissey et al. 2007), the UKIRT Infrared Deep Sky Survey (UKIDSS; Lawrence et al. 2007), and the Wide-field Infrared Survey Explorer (*WISE*; Wright et al. 2010). We show a blackbody curve of 10 000 K, corrected for the expected amount of reddening and arbitrarily scaled to match the optical data. An infrared excess can be seen in both UKIDSS and *WISE* data. As the helium-atmosphere accreting white dwarf should be well approximated by the blackbody, and the accretion disc should be of a similar temperature, it is likely that the infrared excess comes from the donor star. We also plot a second blackbody, with a radius equal to the Roche lobe radius predicted by equation (5) and a temperature of 1850 K (chosen to fit the infrared data). At this temperature the donor would be approximately L4 spectral type. The sum of the two blackbodies is a reasonable fit for all data. If our interpretation is correct, it is the first published direct detection of light from the donor star in a non-direct impacting AM CVn binary. However, while we consider the above to be the most likely interpretation, we caution that some non-thermal component originating at the accretion disc could also result in this SED.

3.2 ASASSN-14ei

ASASSN-14ei (also known as OX Eri) is an AM CVn binary, first detected in superoutburst by ASAS-SN in 2014 July (Prieto et al. 2014). Follow-up observations reported by Prieto et al. (2014) include a spectrum showing He I and He II lines, as well as optical, UV, and X-ray imaging with *Swift*, and a series of rebrightenings following the original outburst. VSNET alert #17575[2] reported a photometric period during outburst of 41.63(3) min, believed to be a superhump period. Based on archival data from the CRTS, they suggest a photometric period of ≈40.0 min during quiescence, possibly the orbital period.

3.2.1 *Long-term light curve*

The long-term light curve of ASASSN-14ei is shown in Fig. 1. There are several unusual features in the long-term light curve of ASASSN-14ei. No outburst activity is detected during the CRTS coverage before the 2014 superoutburst. Then, following the original superoutburst in 2014, a series of 12 echo outbursts were seen and were followed by the AAVSO. Since the end of the echo outbursts, a number of standard outbursts have been seen with a recurrence time of less than 100 d, shorter than is generally seen in AM CVn binaries. In addition, since the superoutburst, the magnitude of the system between outbursts (in both ASAS-SN and AAVSO data) is brighter than the CRTS magnitude before superoutburst by around 1 mag. We will discuss each of these features in turn.

The series of 12 echo outbursts following the 2014 superoutburst were observed intensively by the AAVSO. The light curve of these outbursts is shown in Fig. 10. Such a large number of echo outbursts is highly unusual, having been seen in only one previous system, WZ Sge (Patterson et al. 2002). It can be seen in the top panel of Fig. 10 that the time separation of these echo outbursts increases over time. In the bottom right panel of Fig. 10 we show the separation between each measured echo outburst. The separation between outbursts increases approximately linearly with the elapsed time since the original superoutburst.

During these echo outbursts, a roughly sinusoidal variation in brightness is seen. In order to measure the period of this signal, we divided the available AAVSO data by observer and then by night. For each of the resulting sections, a Lomb-Scargle periodogram was produced. From all of the periodograms produced in this way, we selected those in which the signal was visible. The mean period from these nights was 42.85 ± 0.14 min, where the uncertainty is the standard error on the mean ($\sigma/\sqrt{N}$).

Following the 2014 superoutburst, the system appears quite different to its state before the superoutburst, being around 1 mag brighter (though note that CRTS uses a clear filter whereas ASAS-SN uses *V*-band and g'-band filters) and showing frequent, normal outbursts (ie. not superoutbursts) which were not seen before 2014. The increase in magnitude can be explained by heating of the central white dwarf. However, the increase in outburst rate is harder to explain. One possible explanation is that the 2014 superoutburst changed the state of the system in such a way that the accretion rate has increased. Several sources have previously suggested that mass transfer rate in hydrogen-dominated CVs may increase via irradiation of the donor, and the phenomenon was invoked by Kotko et al. (2012) to explain various properties of AM CVn superoutburst lightcurves. However, modelling of the irradiation process raises several concerns, most notably the shielding of the equator of the donor star by the accretion disc, and the difficulty of transferring any heating from the higher latitudes of the donor to the equator (Osaki & Meyer 2003, 2004).

Following this perturbation to the state of the system, there is evidence that ASASSN-14ei is slowly returning to the quiescent state that it was in before the 2014 superoutburst. The magnitude of the system appears to be fading. Based on the ASAS-SN *V*-band data (spanning 1300 d, the longest available stretch of data

[2] http://ooruri.kusastro.kyoto-u.ac.jp/mailarchive/vsnet-alert/17575

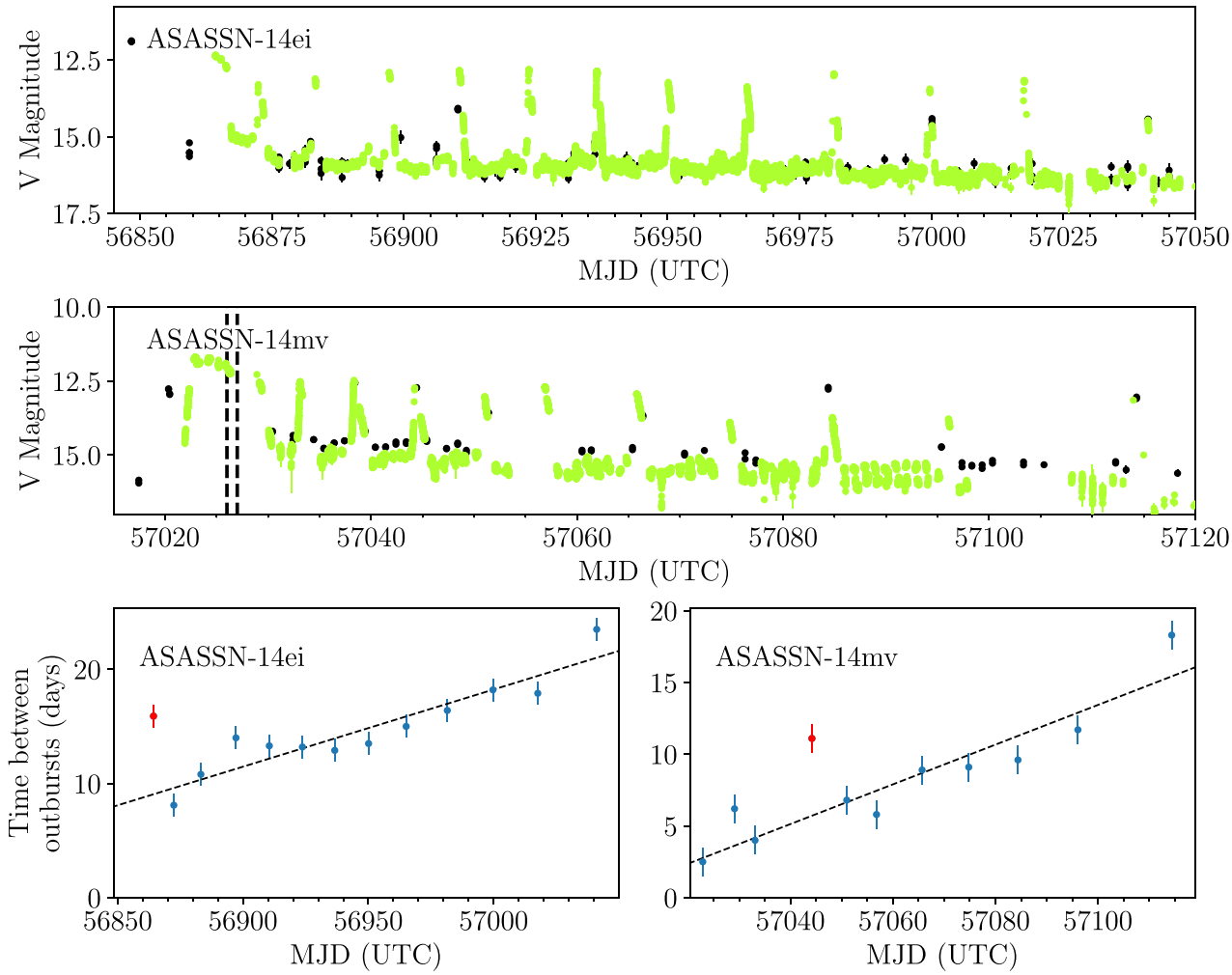

Figure 10. *Top* and *middle*: Echo outburst light curves of ASASSN-14ei and ASASSN-14mv, showing the echo outburst series observed in 2014. Data are coloured according to the scheme in Fig. 1, with green points from the AAVSO and black points from ASAS-SN. Vertical dashed lines show the dates of ULTRASPEC observations of ASASSN-14mv. *Bottom left* and *right*: The time separation between the peak of each detected echo outburst and the peak of its preceding echo outburst. Blue points were used to produce a linear fit (dashed line) while red points were considered outliers and were excluded. The peak of each outburst was selected as the time of the brightest measured AAVSO detection within that outburst. Uncertainties were chosen as ± 1 d, to account for sampling limitations arising from the day/night cycle. In both cases the origin of the x-axis is aligned with the time of the original ASAS-SN detection.

with a consistent observing setup), after masking all outbursts, the brightness is decreasing at a rate of 0.8 ± 0.2 mag yr^{-1}. The frequency of outbursts is also decreasing. In Fig. 11, we show the separation between normal (i.e. non-echo) outbursts as a function of time. While there is considerable scatter, the overall trend appears to be that outbursts are becoming less frequent. Both of these changes would be consistent with a system returning towards its quiescent state after being perturbed to a higher accretion rate during superoutburst.

The above explains an unusual observation noted by Ramsay et al. (2018). That paper found ASASSN-14ei to be unusually bright for its orbital period, with an absolute magnitude $M_g = 8.94$. This absolute magnitude was based on an apparent magnitude from SkyMapper of $g = 15.5$. It can be seen in Fig. 1 that this is brighter than the quiescent magnitude of ASASSN-14ei. We can explain this by noting that the reported epoch of the SkyMapper magnitude measurement is MJD 56963, which was just after the 2014 superoutburst when the brightness of the system was still significantly elevated. A more reliable estimate of the quiescent magnitude can be taken from the CRTS observations before the superoutburst, which have a mean (unfiltered) apparent magnitude of 18.06 mag. This brings the absolute magnitude to $M = 11.5$ mag, very similar to other AM CVn binaries of the same orbital period.

3.2.2 *High-speed photometry*

We obtained high-speed photometry of ASASSN-14ei with ULTRACAM across four nights, one in 2018 January and three in 2018 November (Fig. 12). The system was not in outburst for any of these observations, although a difference in magnitude can be seen between January and November (consistent with the decreasing trend in brightness noted in the previous section).

On January 21, the strongest signal has a period of 44.6 min. Across two consecutive nights, November 9 and November 10, periods can be seen at 86.9 and 88.7 min, respectively. On November 12, this signal is not seen. It may be that the signal from January

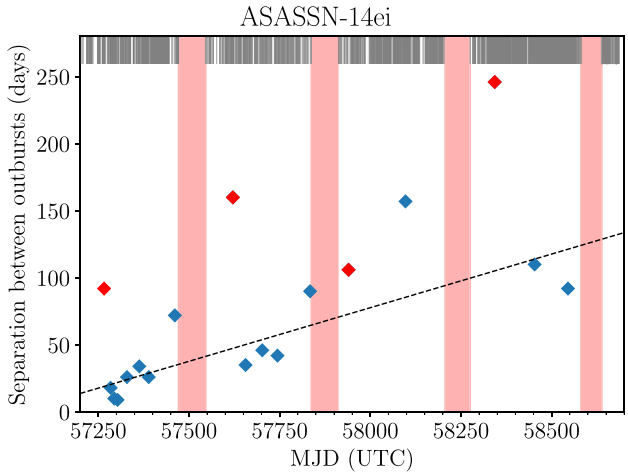

Figure 11. Separations between the times of each normal outburst and its preceding outburst for ASASSN-14ei are shown as blue points. This figure shows isolated outbursts, not including echo outbursts, which were shown in Fig. 10. All outburst detections shown here are from ASAS-SN or AAVSO. Grey vertical dashes at the top of the plot denote the times of ASAS-SN observations; there is no significant decrease in cadence to explain the growing separations of detected outbursts. Red highlighted regions denote significant gaps in coverage due to the star being behind the sun. The data point following each gap has been coloured red to show that it may be unreliable (as preceding outbursts may have been missed during the gap). The dashed black line shows a linear least-squares fit to all blue points, highlighting the trend towards increasing intervals between outbursts.

21 is a harmonic of the signal seen on November 9 and 10, as the periodogram does show a smaller peak at around this frequency. We do not know of any physical process that would produce a signal in the 80–90 min range, but note that AM CVn binaries have been known to show quasi-periodic oscillations at a variety of frequencies (Fontaine et al. 2011). None of these signals is consistent with the periods discussed previously in this paper: neither the period we measured from the AAVSO outburst data (42.85 ± 0.14 min), nor the period measured by VSNET during outburst (41.63 ± 0.03 min), nor the suggested period during quiescence from CRTS (≈40.0 min).

We also note that a signal with a period of approximately 10.5 min appears to be present in data from all four nights. Such a signal could perhaps be related to the spin period of the central white dwarf, but may also be a quasi-periodic oscillation.

3.2.3 Spectroscopy

The mean X-shooter spectrum of ASASSN-14ei is shown in Fig. 2. A series of helium emission lines are seen, including both He I and He II. Several metal lines are also seen, including calcium, nitrogen, and silicon in emission and magnesium and sodium in absorption. The nitrogen lines are notably weaker than in SDSS J1505+0659. The presence of magnesium absorption is interesting. A trailed spectrum shows no notable velocity excursions from the magnesium triplet, suggesting that it originates from the central white dwarf. This may imply a low temperature for the central white dwarf, given the low ionization energy of magnesium. If the mass transfer rate of the system is indeed elevated as suggested in the previous section, this low temperature would be unexpected.

Trailed spectra of some helium lines show marginally visible S-waves from the bright-spot (Fig. 13). Each individual spectrum

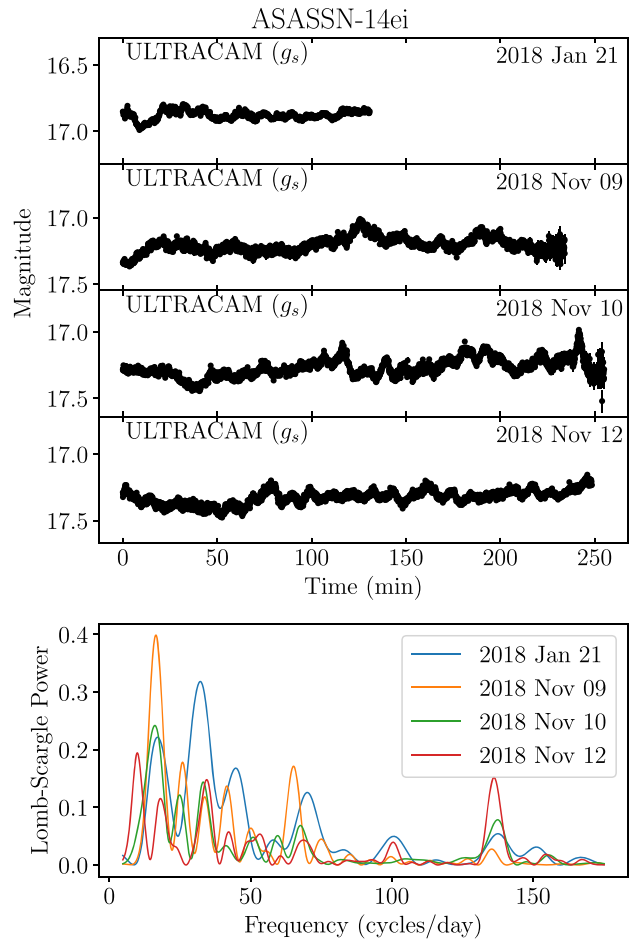

Figure 12. *Upper panels:* ULTRACAM photometry of ASASSN-14ei from four nights. *Lower panel:* Lomb–Scargle periodograms of the data shown in the upper panels, after first subtracting a three-term polynomial.

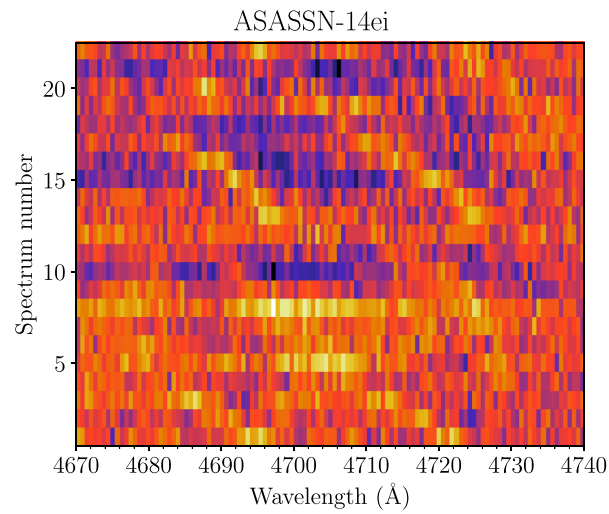

Figure 13. Trailed spectra of the He II 4686 Å and He I 4713 Å lines in ASASSN-14ei, spanning an observation window of 120 min. Each spectrum has been mean subtracted. At some phases, weak S-waves can be seen in both lines (visible as signals moving in parallel) resulting from the bright-spot of the system.

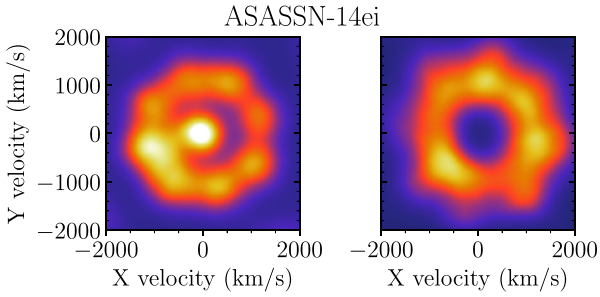

Figure 14. Doppler maps of ASASSN-14ei produced simultaneously from the 4686 Å He II line *(left)* and the 4713 Å He I line *(right)*. Regularly spaced artefacts around the accretion disc result from aliasing between the observation times of the spectra and the orbital period. The He II line features a strong central spike, an accretion disc, and possibly a bright-spot on the left-hand side. The He I line shows accretion disc emission, but no central spike. There may be also be a bright-spot on the left-hand side.

has been continuum and mean subtracted, in order to remove stationary components (including the accretion disc) and highlight the velocity-varying bright-spot. The period of these S-waves is roughly consistent with the orbital period of ≈40 min proposed previously. Unfortunately the bright-spot is not strong enough to be detected by the cross-correlation method used for SDSS J1505+0659.

In order to explore the orbital period, Doppler maps were produced for a range of periods between 38 and 43 min. Each map was inspected visually in order to determine those maps in which the bright-spot was most clearly visible. Such a qualitative approach is clearly not ideal; however, aliasing between the cadence of observations and the orbital period produces artefacts in the maps which are likely to confound quantitative measures such as entropy (Wang et al. 2017, 2018). Our preferred maps had orbital periods in the range of 41–42.5 min. In Fig. 14 are shown Doppler maps produced using a period of 41.6 min.

The orbital periods preferred by this Doppler tomography method are slightly longer than the CRTS photometric orbital period of 40.0 min, and agree better with the proposed superhump period from VSNET of 41.63(3) min. It may be that the modulation reported in VSNET was in fact orbital in origin. Photometric signals at the orbital period can be seen in some systems during some stages of the outburst (e.g. Isogai et al. 2019). However, with the current data we are unable to select between these possible orbital periods.

3.3 ASASSN-14mv

ASASSN-14mv (also known as V493 Gem) was discovered in superoutburst by ASAS-SN in 2014 December (Denisenko et al. 2014). These authors also discussed archival outburst detections from 1938 March (via the Heidelberg Astronomical Plates), 1991 March (via the Palomar Observatory Sky Survey II), and 2011 January (via the MASTER robotic network). The 2011 outburst is also visible in CRTS and PanSTARRS data (see Fig. 1). During the 2014–2015 outburst, photometric periods of 41.8 (Stage A) and 41.0 min (Stage B) were reported by VSNET alert #18124.[3]

[3] http://ooruri.kusastro.kyoto-u.ac.jp/mailarchive/vsnet-alert/18124

3.3.1 *Long-term light curve*

The long-term light curve of ASASSN-14mv is reproduced in Fig. 1. Note that the data from ASAS-SN are affected by a systematic offset of 2.5 mag. Data from other sources (CRTS, PanSTARRS, AAVSO, *Gaia*, and ULTRASPEC, many of these concurrent with the ASAS-SN data) all agree with each other that the quiescent magnitude of the binary is around 18th magnitude, while ASAS-SN measures the quiescent magnitude as 15.5. For several other stars within 20 arcsec, we compared the ASAS-SN and *Gaia* magnitudes, and found the same 2.5 mag offset. We therefore conclude that some unknown systematic problem is affecting ASAS-SN measurements of stars in this field. Given that there are seven stars within 11 arcsec of ASASSN-14mv, and the pixel size of ASAS-SN is 8 arcsec, it is possible that poor seeing may cause some contamination from nearby stars. We therefore discount the ASAS-SN data of this target.

Like ASASSN-14ei, ASASSN-14mv underwent a series of echo outbursts. In this case, 10 rebrightenings followed the original superoutburst. These outbursts were followed by the AAVSO, whose data are reproduced in Fig. 10. As we noted for ASASSN-14ei, the separation between these echo outbursts increases over time, following an approximately linear trend when plotted against the total time elapsed since the original superoutburst. The trend is not strict, however. The fourth rebrightening (marked in red in the bottom right panel of Fig. 10) comes approximately twice as late as expected. The coverage by AAVSO makes it clear that no rebrightening was missed between the third and fourth, meaning that this delay is genuine. Apart from this outlier, the trend is followed remarkably well.

No outbursts of ASASSN-14mv have been detected since the 2014 superoutburst and its rebrightenings, in stark contrast with ASASSN-14ei. Without reliable ASAS-SN measurements, we have limited constraints on how quickly the system returned to its quiescent magnitude. We can say that it had returned to its quiescent magnitude by the time of the ULTRASPEC observation in 2017, some 1000 d following the 2014 superoutburst. (Although the filters are different, the 2017 ULTRASPEC *KG5* observations are a similar magnitude to quiescent observations in the Pan-STARRS *g* and *r* bands, which cover a similar wavelength range.) Following the previous outburst in 2011, we can say that the system returned to its quiescent magnitude after at most 320 d, based on CRTS observations. This behaviour can also be contrasted with ASASSN-14ei, which has remained at an elevated brightness for over 1500 d. Given that the systems appear similar in other ways (similar orbital periods, and both show a similar pattern of rebrightenings immediately following superoutburst), these differences in long-term behaviour is interesting to note.

We searched the AAVSO data during outburst for periodic signals following the methodology described for ASASSN-14ei. The signals we detect have a mean value of 40.9 ± 0.3 min, which is consistent with the superhump modulation reported by VSNET.

3.3.2 *High-speed photometry*

We observed ASASSN-14mv using ULTRASPEC on two consecutive nights during the 2014–2015 superoutburst, and three nights in quiescence in 2017–2018. These data are shown in Fig. 15.

During outburst, strong modulations are seen on both nights, with periods of 40.2 and 36.2 min. During quiescence, on two consecutive nights in 2018 February, a weaker but significant

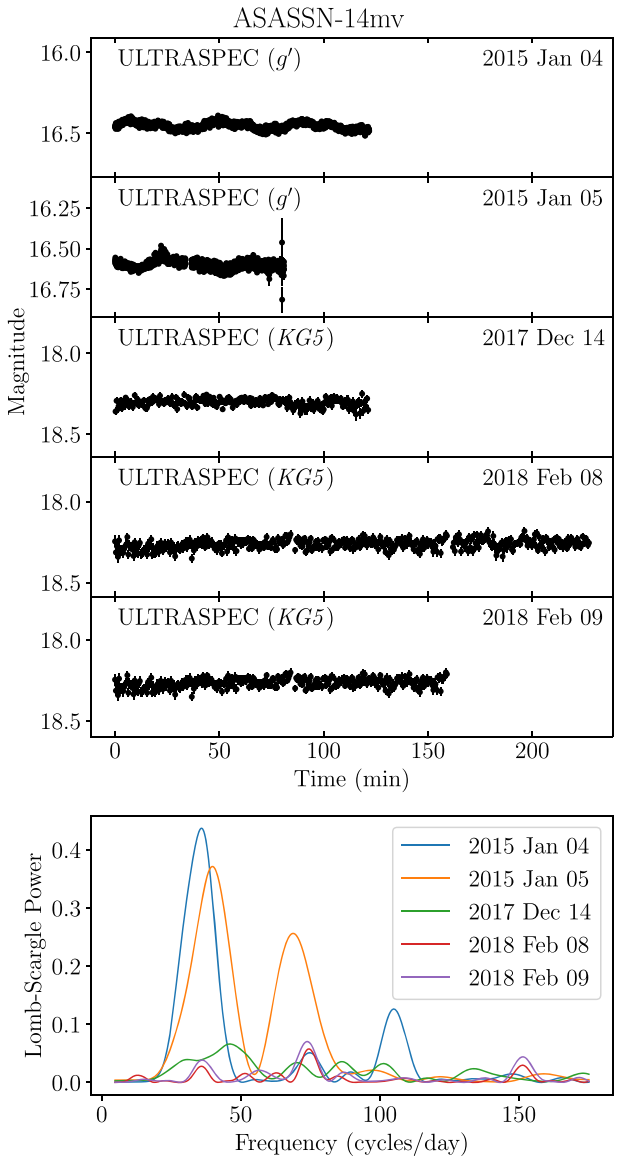

Figure 15. *Upper panels:* ULTRASPEC photometry of ASASSN-14mv from five nights. The 2015 data were obtained during superoutburst, whereas the 2017 and 2018 data were obtained during quiescence. *Lower panel:* Lomb–Scargle periodograms of the data shown in the upper panels, after first subtracting a three-term polynomial.

signal can be seen with periods of 40.2 and 39.8 min. Apart from the January 5 signal, these periods are all consistent with the period detected in the AAVSO data. The January 5 signal has a slightly shorter period, but given the relatively short timespan of the observations on that night this may not be a significant difference. As this modulation was most strongly seen in outburst, it is likely to be a superhump signal. It is consistent with the Stage B superhump period reported by VSNET.

3.3.3 Spectroscopy

The mean spectrum of ASASSN-14mv is shown in Fig. 4. It shows a typical AM CVn spectrum consisting of a series of He I and metal emission lines imposed on a blue continuum. The metals present include calcium, sodium, and nitrogen. The nitrogen emission is relatively strong when compared to ASASSN-14ei. The line profiles are narrow compared to other systems (Fig. 5), suggesting a relatively face-on orbital inclination. Due to the long exposure times used, the orbital RV shifts of the binary are not measurable.

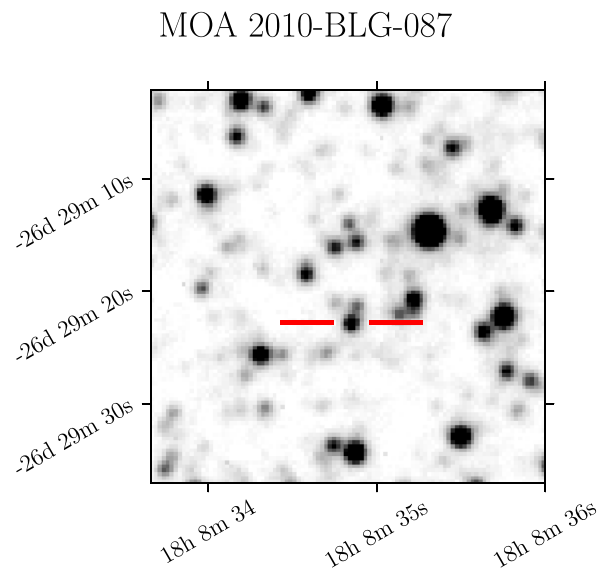

Figure 16. Finder chart for MOA 2010-BLG-087, created from one hour of ULTRACAM g'-band data on April 21. The seeing was 1 $^{\text{arcsec}}$. Note that the target was still in outburst and so appears brighter than its usual level.

3.4 MOA 2010-BLG-087

MOA 2010-BLG-087 was detected during outburst in 2010 by the Microlensing Objects in Astrophysics (MOA) survey of the Galactic bulge. Follow-up photometry showed variability on a period of approximately 50 min, and a spectrum during outburst showed a series of helium lines, suggesting an AM CVn nature for the object (K. Horne, private commumnication). The target is in a crowded region of sky, complicating follow-up. Fig. 16 shows a finder chart, produced from a clipped-mean combination of ULTRACAM images with 1 arcsec seeing. Note that these images were taken during outburst, and so the target was unusually bright at this time.

3.4.1 Spectroscopy

The spectrum of MOA 2010-BLG-087 (Fig. 3) is not typical for an AM CVn binary. Instead it appears similar to a K-type star. We have visually inspected the acquisition images taken prior to these data, and are reasonably confident that the correct target was observed. We suggest that the target is blended with a nearby K star in all ground-based observations to date. During outburst the AM CVn binary was the dominant source, while in quiescence the nearby star dominated.

3.4.2 High-speed photometry

We obtained photometry using ULTRACAM on three nights in 2010 April (Fig. 17). The target was still at an elevated brightness, and the second night (April 22) coincided with an echo outburst

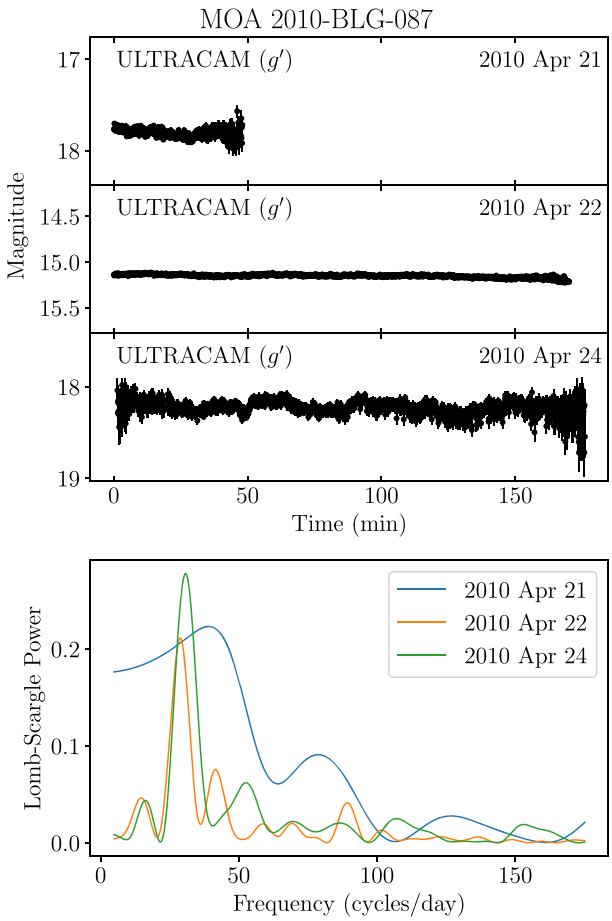

Figure 17. *Upper panels:* ULTRACAM photometry of MOA 2010-BLG-087 from three nights. These observations were made shortly after outburst, and an echo outburst took place on April 22. *Lower panel:* Lomb–Scargle periodograms of the data shown in the upper panels, after subtracting a flat baseline (April 21, due to its shorter coverage) or a three-term polynomial (April 22 and 24). The signal strengths between April 22 and 24 are comparable in terms of absolute flux, but the increased total brightness of the system on April 22 causes the signal to appear weaker on a magnitude scale.

that made the target three magnitudes brighter than April 21 and April 24. Modulations with periods of 49.9 and 46.9 min are visible on April 22 and 24, respectively. Given the short observation window on April 21, a similar signal would not be detected.

For two unresolved stars where one is variable, there will be a correlation between total brightness and the centroid position of the blended object. We compared the x- and y-offsets in pixels of the target from the nearby comparison star (J2000 coordinates 18:08:35.3–26:29:14.7) on the nights of April 22 and 24. The y-offset was particularly strongly correlated with g'-band magnitude. Based on a Pearson's R test, the two-tailed probabilities of such correlations occurring in an uncorrelated sample were $<10^{-26}$ and $<10^{-75}$, for April 22 and 24, respectively. We also found a correlation between g'-band magnitude and g'–r' colour, giving two-tailed probabilities of $<10^{-18}$ and $<10^{-44}$. We therefore believe that the target AM CVn is blended with a nearby source.

In *Gaia* Data Release 2 (Gaia Collaboration 2018), two objects are resolved at these coordinates with a separation of 2 arcsec and magnitudes of $G = 18.3$ and 19.4. While it is tempting to suggest that these may be the two objects which are blended from the ground, we do not believe this to be the case, as a separation of 2 arcsec should be easily resolved by ULTRACAM. We note that a nearby star is visible approximately 2 arcsec north of the target in Fig. 16.

MOA 2010-BLG-087 is the second AM CVn binary to have a co-aligned, late-type, main-sequence star, after V407 Vul. For V407 Vul it is not known whether the co-aligned G-type star is a companion in a tertiary system or is aligned by coincidence, as the sky separation appears very small (0.027 arcsec; Barros et al. 2007).

3.5 CRTS J1028–0819

CRTS J1028–0819 (also known as CSS 090331) was discovered in outburst by CRTS in 2009. A Stage B superhump period of 54.9 ± 0.2 min was measured during outburst (Kato et al. 2009). Woudt et al. (2012) measured a photometric period during quiescence of 52.1 ± 0.6 min, which they suggest to be the orbital period. These photometric measurements suggest that CRTS J1028–0819 is the He CV with the shortest orbital period.

3.5.1 Long-term light curve

The long-term light cure of CRTS J1028–0819 (Fig. 1) shows a series of outbursts with an approximate recurrence time of 210 d. An AM CVn binary at this orbital period would be expected to have a very low accretion rate. As such the presence of any outbursts would be remarkable, and if they did occur the expected recurrence time would be significantly longer (Levitan et al. 2015). In terms of outbursts, it seems this He CV acts very unlike an AM CVn binary.

3.5.2 Spectroscopy

The mean spectrum of CRTS J1028–0819 is shown in Fig. 2. It shows a series of hydrogen and helium emission lines, as well as emission from calcium, sodium, magnesium, and nitrogen. CRTS J1028–0819 shows He II emission at 4686 Å.

Trailed spectra of the H α line in CRTS J1028–0819 are shown in Fig. 18. The system does not appear to show any bright-spot S-wave, and no central spike is visible. In order to search for RV variations, the H α line in each spectrum was cross-correlated with a Gaussian function, fixed such that its full-width at half-maximum was 1600 km s^{-1}. The resulting RV measurements are shown in Fig. 19. A sinusoidal MCMC fit to these measurements produces a period of 53.4 ± 1.3 min, consistent with the photometric periods measured by Kato et al. (2009) and Woudt et al. (2012).

If we follow the interpretations of Kato et al. (2009) and Woudt et al. (2012) and take 52.1 min as the orbital period and 54.9 min as the stage B superhump period, equation (2) gives $q = 0.25 \pm 0.06$, which falls within the range of q measurements for other He CVs.

3.6 V418 Ser

V418 Ser was classed as a dwarf nova following its outburst in 2004 (Rykoff et al. 2004) but few follow-up observations were performed at the time. Following a CRTS-detected outburst in 2014, photometry showed the system to have a superhump period of ≈64.3 min (Kato, Hambsch & Monard 2015a). A spectrum reported by Garnavich et al. (2014) detected the presence of hydrogen.

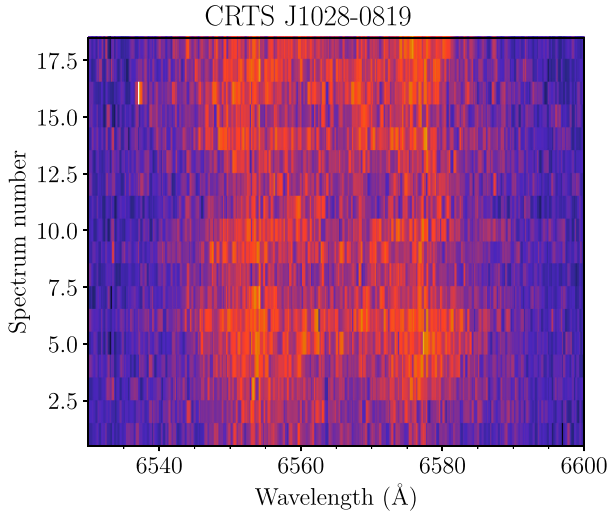

Figure 18. Trailed spectra of the H α emission line of CRTS J1028–0819, spanning 120 min. Each spectrum has been continuum subtracted.

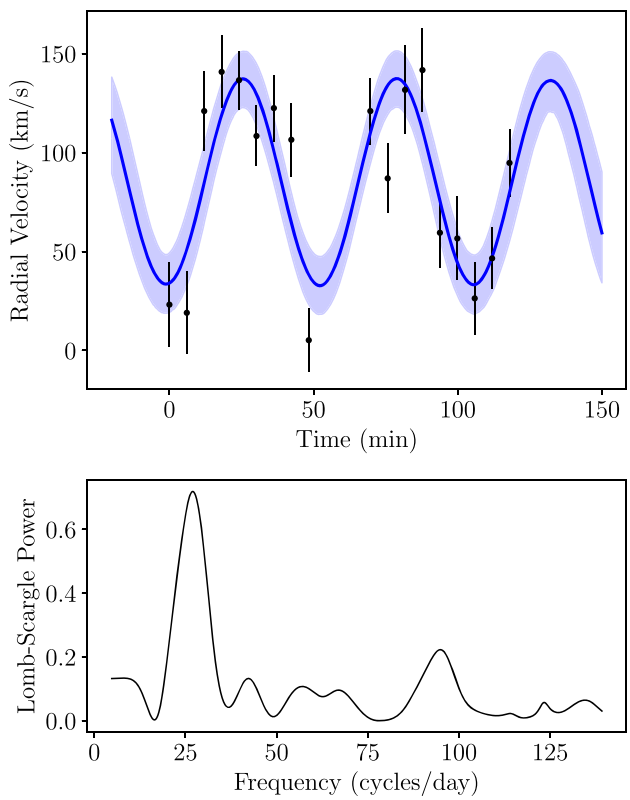

Figure 19. *Above:* RV measurements of the H α line in CRTS J1028–0819, measured by cross-correlating a Gaussian function with the emission lines. A sinusoidal fit is shown, with a period of 53.4 ± 1.3 min. The shaded region shows the 2σ range of expected values produced by the MCMC fit. *Below:* A Lomb–Scargle plot produced from these RV measurements.

3.6.1 *Long-term light curve*

The long-term light curve of V418 Ser (Fig. 1) shows a series of outbursts. The recurrence time is approximately 360 d, with a reasonable amount of scatter. As was the case for CRTS J1028–0819, the presence of outbursts marks a clear departure from the behaviour that would be expected of an AM CVn binary at this orbital period.

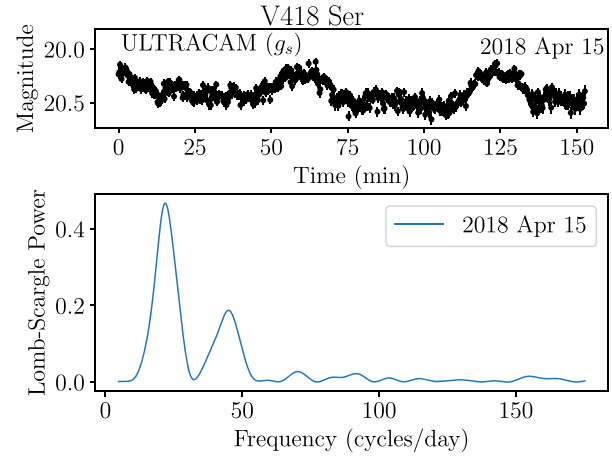

Figure 20. *Above:* ULTRACAM photometry of V418 Ser. *Below:* Lomb–Scargle periodogram of the data in the upper panel.

3.6.2 *Spectroscopy*

The mean FORS2 spectrum is shown in Fig. 3. The system shows a series of emission lines from hydrogen and helium. Emission is also seen from magnesium. The H β line shows a notable absorption wing on its blueward side (the redward wing is hidden by nearby He I emission). The breadth of this absorption suggests it originates from the white dwarf photosphere. No absorption wings are visible around the helium lines.

Trailed spectra of V418 Ser show no visible S-wave from any bright-spot or central spike, and no RV excursions were measurable for any emission line. The lack of any visible velocity excursions in V418 Ser suggests a low-mass donor star. This would imply a low mass-transfer rate, perhaps explaining the lack of any detectable bright-spot in the spectroscopy. The visibility of photospheric hydrogen absorption may imply that the disc is unusually faint relative to the accreting white dwarf, which would also be consistent with a low accretion rate into the disc.

3.6.3 *High-speed photometry*

We obtained 2.5 h of photometry of V418 Ser using ULTRACAM on 2018 April 15 (Fig. 20). The light curve shows a feature resembling an orbital 'hump' (centred on 60 min and again on 125 min in Fig. 20). Similar features are seen in a number of CVs and result from the non-isotropic nature of emission from the bright-spot (e.g. Wood et al. 1986) The presence of such a signal generally implies a relatively edge-on orbital inclination. However, if this signal does result from the bright-spot, it is difficult to reconcile its strength with the weakness of the bright-spot in spectroscopy.

The period of this modulation is 65.9 ± 0.6 min, where the uncertainty was estimated by fitting a sinusoid to the data. This is similar to the superhump period observed by Kato et al. (2015a), but slightly longer. As no uncertainty was reported on the superhump period, we are unable to say if the two periods are consistent. If not, this may be an example of a system with negative superhumps – a superhump signal for which the period is slightly shorter than

the orbital period rather than longer. Negative superhumps originate from nodal precession of an eccentric disc (as opposed to apsidal precession in the positive superhump case) and are observed in a minority of superhumping systems (Hellier 2001).

4 DISCUSSION

4.1 Photometric behaviour

As discussed in Section 3.2, the photometric behaviour of ASASSN-14ei is remarkable. The increased brightness and increased rate of outbursts following the 2014 superoutburst of ASASSN-14ei strongly suggest that the mass transfer rate increased in response to the 2014 superoutburst, perhaps due to heating of the donor star. The system seems even more remarkable when compared to ASASSN-14mv. The two systems appear to be similar in most measurable ways (the orbital periods and outburst magnitudes are similar, and both show the same echo outburst behaviour). Why then does ASASSN-14ei show an increase in mass transfer rate while ASASSN-14mv does not? This difference in behaviour may hint at some underlying difference in the nature of the two binaries, perhaps in the nature of the donor stars.

Leaving ASASSN-14ei aside, there is a stark difference between the outburst behaviour of the AM CVn binaries in this sample (which undergo outbursts rarely if at all) and that of the He CVs (which undergo outbursts with recurrence time-scales on the order of 100 s of d). The more frequent outbursts of the He CVs are likely due to higher accretion rates, resulting from higher mass donors.

4.2 Evolutionary natures

One of the motivations behind this paper was to examine the possibility of an evolutionary link between AM CVn binaries and He CVs. A key signifier of the evolutionary history of these binaries is the donor mass and radius. In Fig. 21, we show the donor masses and radii for all AM CVn binaries and He CVs with appropriate measurements. AM CVn measurements are taken from Green et al. (2018b, their table 4 and references therein), and He CV measurements from the sources listed in Table 1. For the majority of these binaries only the mass ratio is known. For these binaries we assume $M_1 = 0.7 \pm 0.1 M_\odot$. Uncertainties are plotted diagonally due to the tight correlation between donor mass and radius, originating from the relationship between orbital period and donor mean density (Faulkner, Flannery & Warner 1972). By this relationship, binaries with the shortest orbital periods will appear in the bottom right of the figure, while the longest orbital periods would appear in the top left. On the same figure, we plot mass–radius evolutionary tracks for AM CVn binaries descended from the white dwarf donor channel (Deloye et al. 2007), the helium star donor channel (Yungelson 2008), and the evolved CV channel (Goliasch & Nelson 2015).

The two populations follow different distributions. He CVs are constrained to the 50–70 min orbital period range, but their distribution extends to much higher donor masses than AM CVn binaries of the same orbital period. There is, however, a region of mass–radius space in which low-mass He CV donors overlap with long-period AM CVn donors. The He CV CRTS J1122–1110 and the AM CVn binaries Gaia14aae, SDSS J0902+3819, and V396 Hya are all close to this region of overlap.

The q measurements made in this paper are highlighted in red in Fig. 21. CRTS J1028–0819 appears to be towards the high-donor mass end of the distribution of He CVs, as would be expected based on its relatively high outburst rate. SDSS J1505+0659 appears

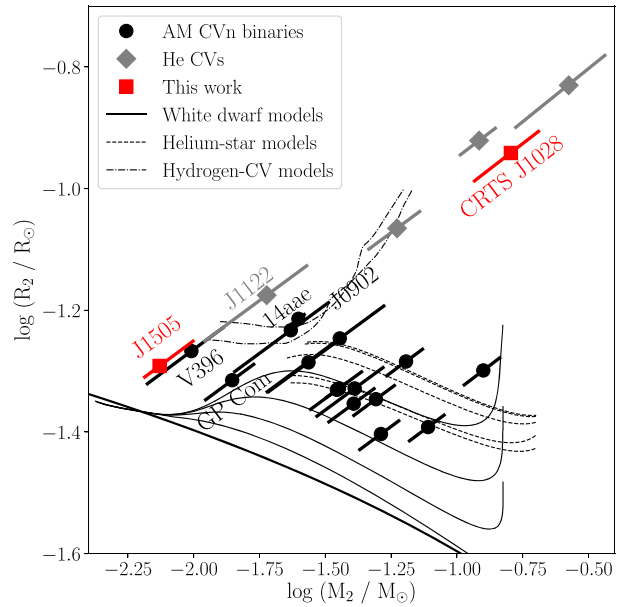

Figure 21. The positions of known AM CVn binaries and He CVs in donor mass–radius space. AM CVn data are taken from (and references therein Green et al. 2018b), and He CV data are from the references in Table 1. The q measurements made in this work are highlighted in red and labelled. Model evolutionary tracks shown are taken from white dwarf donors (Deloye et al. 2007), helium star donors (Yungelson 2008), and evolved CVs (Goliasch & Nelson 2015).

to have a very similar donor to the next-longest-period AM CVn binary, V396 Hya. Looking at the five longest-period AM CVn binaries (five left most in Fig. 21), one could suggest a bifurcation in their radius distribution. SDSS J1505+0659, V396 Hya and GP Com all appear to have significantly smaller radii for their orbital period than Gaia14aae and SDSS J0902+3819, which are more inflated. Such a bifurcation is merely suggestive and is not detected to any significance given the uncertainties on these measurements.

5 CONCLUSIONS

We have presented a spectroscopic and photometric study of six accreting binary systems with orbital periods shorter than the period minimum for hydrogen-accreting CVs. Four of these binaries are of the AM CVn type, and two are He CVs. Four of these binaries have measured orbital periods, and four have measured superhump periods, either resulting from our observations or previously published. In Table 5 we present our period measurements. The binaries in this sample include the AM CVn binary with the longest known orbital period (SDSS J1505+0659 at 67.8 ± 2.2 min) and the He CV with the shortest known orbital period (CRTS J1028–0819 at 53.4 ± 1.3 min).

All but SDSS J1505+0659 have been detected in outburst. The outburst rates of the two He CVs are significantly higher than the outburst rates of the AM CVn binaries, likely due to higher mass donor stars. Two of the AM CVn binaries, ASASSN-14ei and ASASSN-14mv, have notable outburst behaviour, with 12 and 10 echo outbursts, respectively. The mass transfer rate of ASASSN-14ei appears to have increased substantially during the 2014 outburst, causing an increase in brightness and outburst rate. The system has since been gradually returning towards its quiescent state.

Table 5. Orbital periods, superhump periods, and mass ratios for the target systems. Periods are in minutes. Periods marked † are previously published (see the references in relevant sections of the text). For CRTS J1028–0819, we show both the spectroscopic orbital period and the suggested photometric periods.

Target	$P_{\rm orb}$	$P_{\rm sh}$	q
SDSS J1505	67.8 ± 2.2	–	$0.011^{+0.003}_{-0.001}$
ASASSN-14ei	41–42.5	–	–
ASASSN-14mv	–	40.9 ± 0.3	–
MOA 2010	–	≈47–50	–
CRTS J1028	53.4 ± 1.3		
(phot)	52.1 ± 0.6†	54.9 ± 0.2†	0.25 ± 0.06
V418 Ser	65.9 ± 0.6	≈64.3†	–

We measured the mass ratio for SDSS J1505+0659, which has a low-mass donor similar to that of V396 Vul. We also estimate the mass ratio of CRTS J1028–0819 based on previously published photometric periods, and find that it has a high-mass donor, consistent with other He CV measurements. We note that there is some overlap between the regions of donor mass–radius space populated by AM CVn binaries and He CVs (Fig. 21), but the systems studied in this work are not in that region of overlap.

ACKNOWLEDGEMENTS

The authors would like to thank the anonymous reviewer for their feedback. We would also like to thank Christian Knigge and Pier-Emmanuel Tremblay for helpful discussions and comments (during a viva examination!). We acknowledge with thanks the variable star observations from the AAVSO (American Association of Variable Star Observers) International Database contributed by observers worldwide and used in this research, including Franz-Josef Hambsch, Gordon Myers, James Boardman, and David Cejudo Fernandez.

MJG acknowledges funding from STFC (Science and Technology Facilities Council) via studentship grant ST/N504506/1. MJG, TRM, and DS are funded by STFC grant ST/P000495/1. VSD, SPL, ULTRACAM, and ULTRASPEC are funded by STFC via consolidated grant ST/J001589. SGP acknowledges support from the STFC via an Ernest Rutherford Fellowship.

This work is based in part on observations collected at the European Organisation for Astronomical Research in the Southern Hemisphere under ESO programmes 085.D-0541, 095.D-0888, 0100.D-0425, 0101.D-0852, 0102.D-0060, and 0102.D-0953. Data were also obtained using the 2.4 m Thai National Telescope (TNT) operated by the National Astronomy Research Institute of Thailand (NARIT). Further data were obtained under proposal ITP8 using the 4.2 m William Herschel Telescope (WHT), operated by the Isaac Newton Group of Telescopes.

This work made use of software packages SCIPY, NUMPY, ASTROPY, MATPLOTLIB, EMCEE, PAMELA, and MOLLY.

REFERENCES

Abazajian K. N. et al., 2009, ApJS, 182, 543
Appenzeller I. et al., 1998, The Messenger, 94, 1
Armstrong E., Patterson J., Kemp J., 2012, MNRAS, 421, 2310
Augusteijn T., van Kerkwijk M. H., van Paradijs J., 1993, A&A, 267, L55
Augusteijn T., van der Hooft F., de Jong J. A., van Paradijs J., 1996, A&A, 311, 889
Barros S. C. C. et al., 2007, MNRAS, 374, 1334
Breedt E., 2015, Proc.The Golden Age of Cataclysmic Variables and Related Objects - III (Golden2015), Proc. Sci., Trieste, p. 25
Breedt E., Gänsicke B. T., Marsh T. R., Steeghs D., Drake A. J., Copperwheat C. M., 2012, MNRAS, 425, 2548
Breedt E. et al., 2014, MNRAS, 443, 3174
Breivik K., Kremer K., Bueno M., Larson S. L., Coughlin S., Kalogera V., 2018, ApJ, 854, L1
Cannizzo J. K., Nelemans G., 2015, ApJ, 803, 19
Cannizzo J. K., Ramsay G., 2019, AJ, 157, 130
Carter P. J. et al., 2013, MNRAS, 429, 2143
Carter P. J. et al., 2014, MNRAS, 439, 2848
Chambers K. C. et al., 2016, preprint (arXiv:1612.05560)
Chochol D. et al., 2015, Acta Polytech. CTU Proc., 2, 165
Copperwheat C. M. et al., 2011, MNRAS, 410, 1113
Deloye C. J., Taam R. E., Winisdoerffer C., Chabrier G., 2007, MNRAS, 381, 525
Denisenko D. et al., 2014, Astron. Telegram, 6857, 1
Denisenkov P. A., Ivanov V. V., 1987, Sov. Astron. Lett., 13, 214
Dhillon V. S. et al., 2007, MNRAS, 378, 825
Dhillon V. S. et al., 2014, MNRAS, 444, 4009
Dhillon V. et al., 2018, in Christopher E. J., Simard L., Takami T., eds, Proc. SPIE Conf. Ser. Vol. 10702, Ground-based and Airborne Instrumentation for Astronomy VII. SPIE, Belligham, p. 107020L
Drake A. J. et al., 2009, ApJ, 696, 870
Eggleton P. P., 1983, ApJ, 268, 368
Faulkner J., Flannery B. P., Warner B., 1972, ApJ, 175, L79
Fontaine G. et al., 2011, ApJ, 726, 92
Foreman-Mackey D., Hogg D. W., Lang D., Goodman J., 2013, PASP, 125, 306
Gaia Collaboration, 2018, A&A, 616, A1
Garnavich P., Littlefield C., Terndrup D., Adams S., 2014, Astron. Telegram, 6287
Goliasch J., Nelson L., 2015, ApJ, 809, 80
Goodman J., Weare J., 2010, Commun. Appl. Math. Comput. Sci., 5, 65
Green M. J. et al., 2018a, MNRAS, 476, 1663
Green M. J. et al., 2018b, MNRAS, 477, 5646
Green M. J. et al., 2019, MNRAS, 485, 1947
Hardy L. K. et al., 2017, MNRAS, 465, 4968
Hellier C., 2001, Cataclysmic Variable Stars. Springer, Berlin
Iben I. J., Tutukov A. V., 1987, ApJ, 313, 727
Imada A., Isogai K., Yanagisawa K., Kawai N., 2018, PASJ, 70, 79
Isogai K., Kato T., Monard B., Hambsch F.-J., Myers G., Starr P., Cook L. M., Nogami D., 2019, PASJ, 71, 48
Israel G. L., Panzera M. R., Campana S., Lazzati D., Covino S., Tagliaferri G., Stella L., 1999, A&A, 349, L1
Ivanova N. et al., 2013, A&AR, 21, 59
Kato T., Osaki Y., 2013, PASJ, 65, 115
Kato T., Uemura M., Ishioka R., Nogami D., Kunjaya C., Baba H., Yamaoka H., 2004, PASJ, 56, S1
Kato T. et al., 2009, PASJ, 61, S395
Kato T., Hambsch F.-J., Monard B., 2015a, PASJ, 67, L2
Kato T. et al., 2015b, PASJ, 67, 105
Knigge C., 2006, MNRAS, 373, 484
Knigge C., Baraffe I., Patterson J., 2011, ApJS, 194, 28
Kochanek C. S. et al., 2017, PASP, 129, 104502
Kotko I., Lasota J.-P., Dubus G., Hameury J.-M., 2012, A&A, 544, A13
Kremer K., Breivik K., Larson S. L., Kalogera V., 2017, ApJ, 846, 95
Kupfer T., Groot P. J., Levitan D., Steeghs D., Marsh T. R., Rutten R. G. M., Nelemans G., 2013, MNRAS, 432, 2048
Kupfer T. et al., 2015, MNRAS, 453, 483
Kupfer T., Steeghs D., Groot P. J., Marsh T. R., Nelemans G., Roelofs G. H. A., 2016, MNRAS, 457, 1828
Kupfer T. et al., 2018, MNRAS, 480, 302
Lasota J.-P., 2001, New Astron. Rev., 45, 449
Lawrence A. et al., 2007, MNRAS, 379, 1599
Levitan D., Groot P. J., Prince T. A., Kulkarni S. R., Laher R., Ofek E. O., Sesar B., Surace J., 2015, MNRAS, 446, 391

Littlefield C. et al., 2013, AJ, 145, 145
Lomb N. R., 1976, Ap&SS, 39, 447
Longstaff E. S., Casewell S. L., Wynn G. A., Page K. L., Williams P. K. G., Braker I., Maxted P. F. L., 2019, MNRAS, 484, 2566
Marsh T., 2019, , Astrophysics Source Code Library, record ascl:1907.012
Marsh T. R., Horne K., 1988, MNRAS, 235, 269
Marsh T. R., Horne K., Schlegel E. M., Honeycutt R. K., Kaitchuck R. H., 1990, ApJ, 364, 637
Masci F. J. et al., 2019, PASP, 131, 018003
McAllister M. et al., 2019, MNRAS, 486, 5535
Meyer F., Meyer-Hofmeister E., 2015, PASJ, 67, 52
Morales-Rueda L., Marsh T. R., Steeghs D., Unda-Sanzana E., Wood J. H., North R. C., 2003, A&A, 405, 249
Morrissey P. et al., 2007, ApJS, 173, 682
Motch C., Haberl F., Guillout P., Pakull M., Reinsch K., Krautter J., 1996, A&A, 307, 459
Mowlavi N., 1999, A&A, 350, 73
Nather R. E., Robinson E. L., Stover R. J., 1981, ApJ, 244, 269
Naylor T., 1998, MNRAS, 296, 339
Nelemans G., Yungelson L. R., Portegies Zwart S. F., 2004, MNRAS, 349, 181
Osaki Y., Meyer F., 2003, A&A, 401, 325
Osaki Y., Meyer F., 2004, A&A, 428, L17
Paczyński B., 1967, Acta Astron., 17, 287
Pala A. F. et al., 2020, MNRAS, 494, 3799
Patterson J. et al., 1998, PASP, 110, 1290
Patterson J. et al., 2002, PASP, 114, 721
Patterson J. et al., 2005, PASP, 117, 1204
Pearson K. J., 2007, MNRAS, 379, 183
Podsiadlowski P., Han Z., Rappaport S., 2003, MNRAS, 340, 1214
Prieto J. L. et al., 2014, Astron. Telegram, 6475
Ramsay G. et al., 2014, MNRAS, 438, 789
Ramsay G. et al., 2018, A&A, 620, A141
Rau A. et al., 2009, PASP, 121, 1334
Roelofs G. H. A., Groot P. J., Nelemans G., Marsh T. R., Steeghs D., 2006, MNRAS, 371, 1231
Roelofs G. H. A., Rau A., Marsh T. R., Steeghs D., Groot P. J., Nelemans G., 2010, ApJ, 711, L138
Ruiz M. T., Rojo P. M., Garay G., Maza J., 2001, ApJ, 552, 679
Rykoff E. S. et al., 2004, Inf. Bull. Var. Stars, 5559, 1
Savonije G. J., de Kool M., van den Heuvel E. P. J., 1986, A&A, 155, 51
Scargle J. D., 1982, ApJ, 263, 835
Shappee B. J. et al., 2014, ApJ, 788, 48
Smak J., 1981, Acta Astron., 31, 395
Solheim J.-E., 2010, PASP, 122, 1133
Steeghs D., Marsh T. R., Barros S. C. C., Nelemans G., Groot P. J., Roelofs G. H. A., Ramsay G., Cropper M., 2006, ApJ, 649, 382
Szkody P. et al., 2005, AJ, 129, 2386
Thorstensen J. R., Fenton W. H., Patterson J. O., Kemp J., Krajci T., Baraffe I., 2002, ApJ, 567, L49
Uthas H., Knigge C., Long K. S., Patterson J., Thorstensen J., 2011, MNRAS, 414, L85
VanderPlas J. T., 2018, ApJS, 236, 16
Vernet J. et al., 2011, A&A, 536, A105
Wang L., Steeghs D., Casares J., Charles P. A., Muñoz-Darias T., Marsh T. R., Hynes R. I., O'Brien K., 2017, MNRAS, 466, 2261
Wang L., Steeghs D., Galloway D. K., Marsh T., Casares J., 2018, MNRAS, 478, 5174
Warner B., 1995, Cataclysmic Variable Stars, Cambridge University Press, Cambridge
Wood J., Horne K., Berriman G., Wade R., O'Donoghue D., Warner B., 1986, MNRAS, 219, 629
Woudt P. A., Warner B., 2011, Astron. Telegram, 3705, 1
Woudt P. A., Warner B., de Budé D., Macfarlane S., Schurch M. P. E., Zietsman E., 2012, MNRAS, 421, 2414
Wright E. L. et al., 2010, AJ, 140, 1868
Yungelson L. R., 2008, Astron. Lett., 34, 620